J. Fluid Mech. (2021), *vol.* 0, A1.
Published by Cambridge University Press
doi:10.1017/jfm.2020.810

Shock-induced bubble collapse near solid materials: effect of acoustic impedance

S. Cao[1], G. Wang[1], O. Coutier-Delgosha[1] and K. Wang[1],†

[1]Department of Aerospace and Ocean Engineering, Virginia Tech, Blacksburg, VA 24061, USA

(Received 23 November 2019; revised 20 July 2020; accepted 7 September 2020)

The fluid dynamics of a bubble collapsing near an elastic or viscoelastic material is coupled with the mechanical response of the material. We apply a multiphase fluid–solid coupled computational model to simulate the collapse of an air bubble in water induced by an ultrasound shock wave, near different types of materials including metals (e.g. aluminium), polymers (e.g. polyurea), minerals (e.g. gypsum), glass and foams. We characterize the two-way fluid–material interaction by examining the fluid pressure and velocity fields, the time history of bubble shape and volume and the maximum tensile and shear stresses produced in the material. We show that the ratio of the longitudinal acoustic impedance of the material compared to that of the ambient fluid, Z/Z_0, plays a significant role. When $Z/Z_0 < 1$, the material reflects the compressive front of the incident shock into a tensile wave. The reflected tensile wave impinges on the bubble and decelerates its collapse. As a result, the collapse produces a liquid jet, but not necessarily a shock wave. When $Z/Z_0 > 1$, the reflected wave is compressive and accelerates the bubble's collapse, leading to the emission of a shock wave whose amplitude increases linearly with $\log(Z/Z_0)$, and can be much higher than the amplitude of the incident shock. The reflection of this emitted shock wave impinges on the bubble during its rebound. It reduces the speed of the bubble's rebound and the velocity of the liquid jet. Furthermore, we show that, for a set of materials with $Z/Z_0 \in [0.04, 10.8]$, the effect of acoustic impedance on the bubble's collapse time and minimum volume can be captured using phenomenological models constructed based on the solution of Rayleigh–Plesset equation.

Key words: bubble dynamics, computational methods, cavitation

1. Introduction

The collapse of a bubble near a material surface features a rapid, non-spherical compression of the internal gas, which may release mechanical and thermal energy in the forms of shock wave, liquid jet and increased local temperature. This process is a fundamental event in many science and engineering applications that involve cavitation, either as a harmful byproduct leading to erosion, noise and performance degradation, or as a useful mechanism for desired material modification and fabrication. Within the latter category, it has been demonstrated that the energy pulses released from bubble collapse may be used to remove contaminants or unwanted particles on a surface (Brems *et al.* 2014; Guo *et al.* 2014), fabricate nanostructured solid materials (Xu, Zeiger & Suslick

† Email address for correspondence: kevinwgy@vt.edu

2013), break agglomerates in a liquid metal (Kudryashova & Vorozhtsov 2016), facilitate kidney stone destruction in shock wave lithotripsy (Zhong 2013), increase the permeability of human tissue or cell membrane for targeted drug/gene delivery (Coussios & Roy 2008; Brennen 2015) and mediate cellular mechanotransduction (Li *et al.* 2018) – just to name a few examples. A common issue in these applications is that the location, extent and intensity of cavitation need to be controlled carefully, as the boundary between meritorious effects and deleterious effects can be narrow. For example, using cavitation to remove biofouling on ship hulls needs to avoid damage to hull coatings (Guo *et al.* 2014). In lithotripsy, cavitation bubbles can contribute to stone fragmentation; yet they may also damage human tissue and scatter the focused ultrasound waves (Zhong, Zhou & Zhu 2001; Pishchalnikov *et al.* 2003; Maeda *et al.* 2018). Similarly, the use of cavitation to produce cell sonoporation produces therapeutic effects only when the detrimental side effects due to overdose do not occur (Ohl *et al.* 2006). In general, the need for controlled cavitation bubble collapse near various solid and soft materials calls for improved understanding of the two-way coupling between bubble dynamics and the material's response.

In the past, the non-spherical collapse of a bubble near different types of material boundaries has been studied using experimental and computational methods. The investigated material boundaries include a rigid wall (e.g. Zhang, Duncan & Chahine 1993; Brujan *et al.* 2002; Calvisi, Iloreta & Szeri 2008; Johnsen & Colonius 2009; Brujan & Matsumoto 2012; Wang 2014), a surface of elastic solid bodies (e.g. Brujan *et al.* 2001; Sankin & Zhong 2006), thin films (e.g. Turangan *et al.* 2006), a surface of soft tissues (e.g. Kodama & Takayama 1998) and free liquid–gas interfaces (e.g. Blake & Gibson 1981; Robinson *et al.* 2001). The damage and fracture (e.g. pits, cracks, holes) in a nearby material after multiple cycles of bubble collapse have also been investigated (e.g. Philipp & Lauterborn 1998; Dular, Delgosha & Petkovšek 2013). Nonetheless, knowledge of the dynamic response of different types of materials to bubble collapse – such as the amplitude, profile and propagation of surface and bulk elastic waves – is still limited. In this regard, a few teams (e.g. Freund, Shukla & Evan 2009; Kobayashi, Kodama & Takahira 2011) have applied Eulerian multiphase fluid dynamics solvers to simulate the interaction of collapsing bubbles with soft materials (e.g. biological tissues), in which the materials are modelled as fluids. Turangan *et al.* (2017) have applied a Lagrangian solver to simulate shock-induced bubble collapse near aluminium walls and foils. Chahine & Hsiao (2015) have applied a fluid–solid coupled solver to simulate bubble collapse near metals and polymers, including the resulting permanent deformation (e.g. pitting). Wang (2017) has applied a fluid–solid coupled solver to simulate shock-bubble–stone interaction in the context of shock wave lithotripsy. Moreover, although a few studies using high-speed photography and acoustic measurements have revealed significant impact of the Young's modulus of the material on bubble dynamics (e.g. Gibson & Blake 1982; Brujan *et al.* 2001; Sankin & Zhong 2006), the detailed reciprocal effects of the acoustic, elastic and viscoelastic properties of the material on bubble dynamics are still largely unknown.

In this paper, we present a computational study of shock-induced bubble collapse near different solid materials, focusing on describing the two-way fluid–material interaction and investigating the effect of the material's acoustic impedance. Specifically, we consider an air bubble in water next to a planar material boundary. We send an ultrasound shock wave with a sharp compressive front towards the bubble, which drives it to collapse. This setting is relevant to a number of ultrasound applications, and is possible to replicate in a laboratory environment. The acoustic impedance of a material is defined as $Z = \rho c$, where ρ and c denote mass density and acoustic (P-wave) velocity, respectively. Our interest in the effect of Z is motivated by two considerations. First, it is a fundamental material property that can often clearly distinguish different 'hard' and 'soft' materials in an application. Second, a few previous studies on bubble collapse near a rigid wall have indicated that the reflection of the shock wave against a material surface may have significant effects. For example, Calvisi *et al.* (2008) highlighted that the reflected shock against a rigid wall intensifies the non-spherical bubble collapse. The results of Johnsen & Colonius (2009) and Wang (2017) also support this finding. Acoustic impedance is a key parameter in wave reflection and transmission; a rigid wall can be considered as an extreme case with $Z = \infty$. Therefore, the finding mentioned above naturally suggests that it is valuable to investigate real materials with different (and finite) values of Z, including cases where its value is smaller than the acoustic impedance of the ambient fluid.

We employ a recently developed three-dimensional (3-D), multiphase fluid–solid coupled computational framework in this study (Wang, Lea & Farhat 2015; Huang, De Santis & Farhat 2018). The important components of this framework relevant to the present study include: (*a*) an Eulerian finite volume, multiphase compressible Navier–Stokes equation solver, equipped with a level-set method for tracking the surface of the bubble; (*b*) a Lagrangian finite element solid mechanics (elasticity and viscoelasticity) solver; (*c*) an embedded boundary method for tracking the fluid–solid interface in an unstructured, non-interface-conforming fluid mesh (Wang *et al.* 2012; Huang *et al.* 2018); (*d*) the FIVER ('Finite Volume method with Exact multi-material Riemann solvers') method for enforcing the interface conditions at the liquid–gas and fluid–solid interfaces (Wang *et al.* 2011; Farhat, Gerbeau & Rallu 2012; Main *et al.* 2017); and (*e*) a second-order, numerically stable partitioned procedure for coupling the fluid and solid solvers (Farhat *et al.* 2010). This computational framework has been applied to simulate several fluid–structure interaction problems involving shock waves, large structural deformation, instability and fracture (e.g. Farhat *et al.* 2013; Wang *et al.* 2014; Chung *et al.* 2018; Cao *et al.* 2019). It has also been verified and validated for a few two-phase flow problems involving a bubble collapsing near a rigid wall (e.g. Farhat, Rallu & Shankaran 2008; Main *et al.* 2017; Wang 2017). For example, Main *et al.* (2017) simulated a laboratory experiment of underwater bubble implosion, in which the gas content (air) is initially enclosed by a thin-walled glass sphere (Turner 2007). They showed that the simulated pressure time history agrees favourably with the measurement obtained in the laboratory. In this work, we simulate the collapse of a bubble near a broad range of materials including metals (e.g. aluminium), polymers (e.g. polyurea), minerals (e.g. gypsum), glass and foams. In each case, we characterize the two-way fluid–material interaction using fluid pressure, velocity, bubble volume and the maximum tensile and shear stresses in the material. To highlight the effect of acoustic impedance on the dynamics of bubble collapse, we compare the bubble's collapse time, the minimum bubble volume, the jet velocity and the pressure load induced by the emitted shock wave on the material surface.

The remainder of this paper is organized as follows. Section 2 presents the physical model and numerical methods used in this study. Section 3.1 presents a verification of the computational framework using a 3-D benchmark problem featuring wave transmission and deflection at a fluid–solid interface. Section 4 presents the results of shock-induced bubble collapse near three representative materials, focusing on describing the two-way interaction between the fluid dynamics and the response of the material. Furthermore, § 5 presents a parametric study that considers different materials with acoustic impedance ranging from 0.063 to 17.28 MPa·s m^{-1}. We show that the effect of acoustic impedance on the bubble's collapse time and minimum volume can be captured using phenomenological models constructed based on the solution of the Rayleigh–Plesset equation. Finally, we provide a few concluding remarks in § 6.

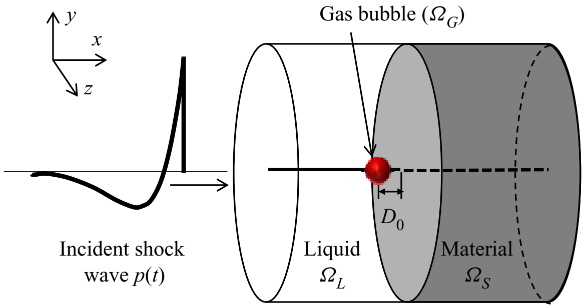

FIGURE 1. A 3-D fluid–solid coupled model of shock-induced bubble collapse near a solid or soft material.

2. Physical model and numerical methods

2.1. *Governing equations and constitutive models*

We consider a 3-D spatial domain comprised of multiple subdomains occupied by different fluid and solid materials. Figure 1 presents a schematic drawing of the problem set-up. A spherical gas bubble with a radius of R_0 is placed in a liquid at a standoff distance D_0 from the solid material (measured from the centre of the bubble). An incident shock wave propagates towards the bubble from the opposite side, causing its collapse. Let Ω_G, Ω_L and Ω_S denote the subdomains occupied by the bubble, the ambient fluid (liquid) and the solid material, respectively. We model both the gas inside the bubble and the ambient fluid as compressible inviscid fluids. Dropping of viscosity can be justified by the high pressure of the incident shock wave in the current problem set-up (see, e.g. Brujan (2019) for a different and more complex fluid environment) and a relatively small time frame considered within this study.

Therefore, in Ω_G and Ω_L, we solve the following Euler equations in the Eulerian frame:

$$\frac{\partial \boldsymbol{W}(\boldsymbol{x}, t)}{\partial t} + \nabla \cdot \mathcal{F}(\boldsymbol{W}) = 0, \quad \forall \boldsymbol{x} \in \Omega_L(t) \cup \Omega_G(t), \ t > 0, \tag{2.1}$$

with

$$\boldsymbol{W} = \begin{bmatrix} \rho \\ \rho \boldsymbol{V} \\ \rho e_t \end{bmatrix}, \quad \mathcal{F} = \begin{bmatrix} \rho \boldsymbol{V}^T \\ \rho \boldsymbol{V} \otimes \boldsymbol{V} + p\boldsymbol{I} \\ (\rho e_t + p)\boldsymbol{V}^T \end{bmatrix}, \tag{2.2a,b}$$

where ρ, $\boldsymbol{V}$, p and e_t denote the fluid density, velocity, pressure and the total energy per unit mass, respectively; $\boldsymbol{I}$ is the 3×3 identity matrix. Equation (2.1) is closed by an equation of state (EOS) for each fluid material. We apply the perfect gas EOS to the gas inside the bubble, i.e.

$$p = (\gamma_G - 1)\rho e, \tag{2.3}$$

where γ_G is the heat capacity ratio, and e is the internal energy per unit mass. In this work, we set $\gamma_G = 1.4$. We assume the ambient fluid is water, and apply the stiffened equation of state, i.e.

$$p = (\gamma_L - 1)\rho e - \gamma_L p_L, \tag{2.4}$$

where $\gamma_L = 6.59$ and $p_L = 410$ MPa (Johnsen & Colonius 2008).

Within the subdomain of the solid material, i.e. Ω_S, we adopt the Lagrangian frame and solve the following equation of motion that enforces the balance of linear momentum:

$$\rho_s \ddot{\boldsymbol{u}}(\boldsymbol{X}, t) - \nabla \cdot \boldsymbol{\sigma}(\boldsymbol{u}, \dot{\boldsymbol{u}}) = \boldsymbol{b}, \quad \forall \boldsymbol{X} \in \Omega_S(0),\ t > 0, \tag{2.5}$$

where $\boldsymbol{u}$ denotes displacement, ρ_s the material's mass density and $\boldsymbol{\sigma}$ the Cauchy stress tensor; $\boldsymbol{b}$ denotes the body force acting in Ω_S, which is assumed to be zero in this study.

We adopt the generalized Maxwell model of viscoelasticity (Cheneler 2016), which combines linear springs and linear dashpots. Assuming zero strain at $t = 0$, the stress at any time instance $t > 0$ can be written in the form of the hereditary integral,

$$\boldsymbol{\sigma}(t) = \int_0^t G_R(t - s) \frac{\mathrm{d}\boldsymbol{\epsilon}(s)}{\mathrm{d}s}\, \mathrm{d}s, \tag{2.6}$$

where $\boldsymbol{\epsilon}$ denotes the strain tensor; $G_R(t)$ is the relaxation modulus. In this work, we express $G_R(t)$ as a Prony series, i.e.

$$G_R(t) = G_0 \left[1 - \sum_{i=1}^{N} g_i (1 - \mathrm{e}^{-t/\tau_i}) \right], \tag{2.7}$$

where $G_0 = G_R(0)$ is the instantaneous modulus, g_i and τ_i are material-specific model parameters. The Prony series is appealing particularly from a numerical viewpoint, as it does not require storing of the time history of strain. Specifically, we compute $\sigma(t)$ using a recursive formula, as shown in Goh, Charalambides & Williams (2004).

For some of the materials investigated in this study (e.g. a strengthened gypsum, metals), the viscoelastic effect of the material is negligible. These materials are modelled essentially by linear elasticity, with constitutive equation

$$\boldsymbol{\sigma} = \frac{E\nu}{(1+\nu)(1-2\nu)} tr(\boldsymbol{\epsilon})\boldsymbol{I} + \frac{E}{1+\nu}\boldsymbol{\epsilon}, \tag{2.8}$$

where E and ν are the Young's modulus and Poisson's ratio of the material, respectively; $tr(\cdot)$ denotes the trace operator.

At the fluid–solid interface, $\Gamma_{FS} = \partial\Omega_S(t) \cap (\partial\Omega_L(t) \cup \partial\Omega_G(t))$, we enforce the continuity of normal velocity and surface traction, i.e.

$$\left.\begin{array}{l} (\boldsymbol{V} - \dot{\boldsymbol{u}}) \cdot \boldsymbol{n} = 0, \\ -p\boldsymbol{n} = \boldsymbol{\sigma}(\boldsymbol{u}, \dot{\boldsymbol{u}}) \cdot \boldsymbol{n}, \end{array}\right\} \quad \text{on } \Gamma_{FS}, \tag{2.9}$$

where $\boldsymbol{n}$ denotes the unit normal to Γ_{FS}.

At the liquid–gas interface, $\Gamma_{FF}(t) = \partial\Omega_L(t) \cap \partial\Omega_G(t)$, we assume that the two fluid materials are immiscible. Also, surface tension is negligible compared to the pressure of the prescribed shock wave. Thus, the interface conditions are those describing a contact discontinuity, i.e.

$$\left.\begin{array}{l} (\boldsymbol{V}_L - \boldsymbol{V}_G) \cdot \boldsymbol{n} = 0, \\ p_L = p_G, \end{array}\right\} \quad \text{on } \Gamma_{FF}. \tag{2.10}$$

2.2. *Fluid–solid coupled computational framework*

We apply a recently developed fluid–solid coupled computational framework to solve the above model equations. The framework couples a finite volume, multiphase compressible

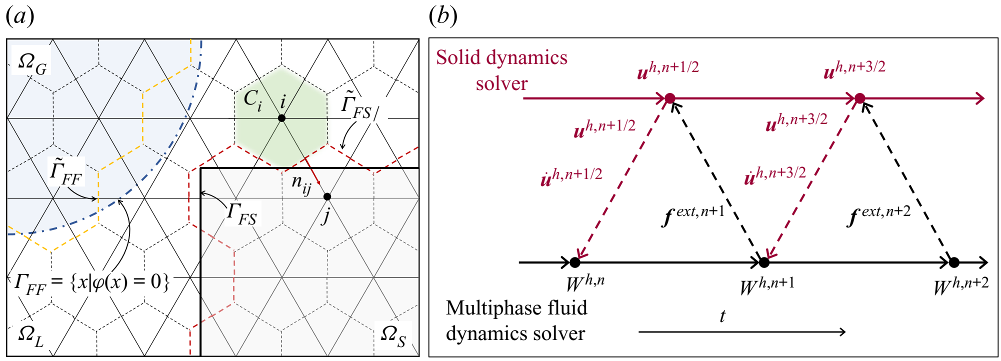

FIGURE 2. Illustration of the spatial (*a*) and temporal (*b*) discretization methods applied in the computational framework.

flow solver with a finite element solid dynamics solver using an embedded boundary method and a staggered partitioned procedure (figure 2).

As illustrated in figure 2(*a*), the fluid governing equations are semi-discretized in an augmented fluid domain, $\tilde{\Omega} = \Omega_L \cup \Omega_G \cup \Omega_S$, using an unstructured, node centred, non-interface-conforming finite volume mesh, denoted by $\tilde{\Omega}^h$. For each node of the mesh (e.g. node i), a dual cell (i.e. control volume) C_i is constructed. Integrating (2.1) within C_i gives

$$\frac{\partial \boldsymbol{W}_i}{\partial t} + \frac{1}{\|C_i\|} \sum_{j \in Nei(i)} \int_{\partial C_{ij}} \mathcal{F}(\boldsymbol{W}) \cdot \boldsymbol{n}_{ij} \, \mathrm{d}S = 0, \tag{2.11}$$

where $\boldsymbol{W}_i$ denotes the average of $\boldsymbol{W}$ in C_i, $\|C_i\|$ denotes the volume of C_i, $Nei(i)$ denotes the set of nodes connected to node i by an edge, $\partial C_{ij} = \partial C_i \cap \partial C_j$ and $\boldsymbol{n}_{ij}$ is the unit normal to ∂C_{ij}. Depending on the location of nodes i and j, four scenarios arise in the calculation of the surface integral over ∂C_{ij}:

(*a*) If nodes i and j belong to the same fluid subdomain (Ω_L or Ω_G), the flux across ∂C_{ij} is calculated using the well-known monotonic upwind scheme conservation law (MUSCL) scheme (Van Leer 1979) and Roe's flux (Roe 1981).

(*b*) If nodes i and j belong to different fluid subdomains (i.e. one in Ω_L, the other in Ω_G), a one-dimensional (1-D) two-fluid Riemann problem is constructed along edge i–j, i.e.

$$\frac{\partial \boldsymbol{w}}{\partial \tau} + \frac{\partial \mathcal{F}(\boldsymbol{w})}{\partial \xi} = 0, \quad \text{with } \boldsymbol{w}(\xi, 0) = \begin{cases} \boldsymbol{w}_i & \text{if } \xi \leq 0, \\ \boldsymbol{w}_j & \text{if } \xi > 0, \end{cases} \tag{2.12}$$

where τ denotes the time coordinate; ξ denotes the spatial coordinate along the 1-D axis aligned with $\boldsymbol{n}_{ij}$ and centred at the midpoint between nodes i and j. The initial states $\boldsymbol{w}_i$ and $\boldsymbol{w}_j$ are projections of $\boldsymbol{W}_i$ and $\boldsymbol{W}_j$ on the ξ axis. Equations (2.10) are enforced at the moving interface for $\tau > 0$. The exact solution of this 1-D Riemann problem is supplied to Roe's flux function to compute the flux across ∂C_{ij} (Farhat *et al.* 2012).

(*c*) If one of the two nodes (e.g. node i) belongs to a fluid subdomain (Ω_L or Ω_G), while the other node belongs to the solid subdomain (Ω_S), a 1-D fluid–solid Riemann problem with a moving wall boundary is constructed, i.e.

$$\frac{\partial \boldsymbol{w}}{\partial \tau} + \frac{\partial \mathcal{F}(\boldsymbol{w})}{\partial \xi} = 0, \quad \tau > 0, \ \xi < v_S \tau, \tag{2.13}$$

$$\boldsymbol{w}(\xi, 0) = \boldsymbol{w}_i, \quad \xi < 0, \tag{2.14}$$

$$v(v_S \tau, \tau) = v_S, \quad \tau > 0, \tag{2.15}$$

where ξ is the spatial coordinate along the normal direction of the fluid–solid interface and centred at the midpoint between nodes i and j. The initial state $\boldsymbol{w}_i$ is the reconstructed fluid state at the interface; v denotes the fluid velocity at the moving wall boundary, and v_S the normal velocity of the wetted surface of the solid structure (i.e. the fluid–solid interface) at its intersection with fluid edge i–j, which is computed by the solid dynamics solver. Similar to the previous case, the exact solution of this 1-D Riemann problem is supplied to Roe's flux function to compute the flux across ∂C_{ij} (Wang *et al.* 2011).

(*d*) If nodes i and j both belong to the solid subdomain (Ω_S), the flux across ∂C_{ij} is set to 0.

The above method is referred to as FIVER (Farhat *et al.* 2012). It is ideally suited for solving the present problem, as the problem involves both multi-fluid (i.e. liquid–gas) and fluid–solid interfaces.

FIVER requires tracking of the liquid–gas and fluid–solid interfaces in the unstructured, non-interface-conforming mesh $\tilde{\Omega}^h$. We track the evolution of the liquid–gas interface by solving the level-set equation,

$$\frac{\partial \phi(\boldsymbol{x}, t)}{\partial t} + \boldsymbol{V} \cdot \nabla \phi = 0, \quad \forall \boldsymbol{x} \in \Omega_L \cup \Omega_G \cup \Omega_S, \tag{2.16}$$

where $\phi(\boldsymbol{x}, t)$ represents the signed shortest distance from $\boldsymbol{x}$ to the interface. In this way, the large deformation and topological changes (e.g. splitting and merging) of the bubble surface are naturally accommodated. To track the fluid–solid interface, we apply a collision-based computational geometry algorithm as presented in Wang *et al.* (2012, 2015).

In this work, (2.16) is recast in the form

$$\frac{\partial \phi}{\partial t} + \nabla \cdot (\phi \boldsymbol{V}) = \phi \nabla \cdot \boldsymbol{V}, \tag{2.17}$$

and solved on the same fluid mesh using a finite volume method. The convection term, $\nabla \cdot (\phi \boldsymbol{V})$, is discretized using the MUSCL scheme with the upwinding flux. The term $\phi \nabla \cdot \boldsymbol{V}$ is added as a source term. Additional numerical details can be found in Main *et al.* (2017) and Main (2014).

A standard Galerkin finite element method is used to semi-discretize the weak form of (2.5), which yields

$$\boldsymbol{M} \frac{\partial^2 \boldsymbol{u}^h}{\partial t^2} + \boldsymbol{f}^{int}\left(\boldsymbol{u}^h, \frac{\partial \boldsymbol{u}^h}{\partial t}\right) = \boldsymbol{f}^{ext}, \tag{2.18}$$

where $\boldsymbol{M}$ denotes the mass matrix, $\boldsymbol{u}^h$ denotes the discrete displacement vector; $\boldsymbol{f}^{int}$ and $\boldsymbol{f}^{ext}$ denote the discrete internal force and external force vector, respectively.

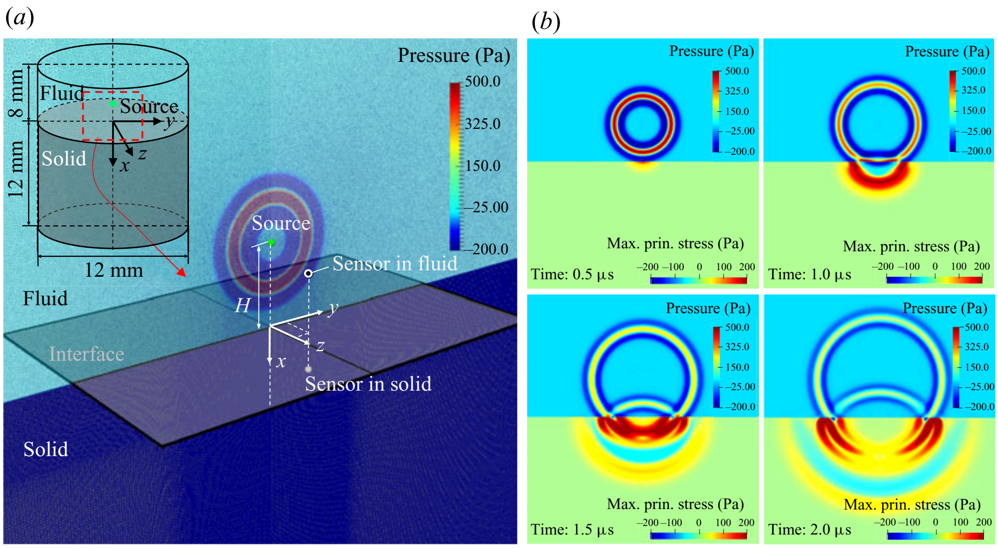

FIGURE 3. (a) Problem set-up (the dynamic pressure of the fluid at $t = 0$ is visualized). (b) Snapshots of numerical solution at four different time instances, showing the dynamic pressure of the fluid and the maximum principal stress in the solid.

We use a staggered fluid–solid time integrator presented in Farhat *et al.* (2010) to advance the fluid and solid subsystems. The fluid subsystem is time integrated using the explicit fourth-order Runge–Kutta scheme, while the solid subsystem is time integrated using the second-order central difference scheme. Notably, the fluid and solid time steps are offset by half a step (figure 2b). This is a designed feature to achieve second-order accuracy in time while maintaining optimal numerical stability.

3. Verification and validation of the computational framework

3.1. *Wave propagation across a plane fluid–solid interface*

We first apply the computational framework described in § 2.2 to solve a 3-D model problem featuring the propagation of an impulsive pressure wave across a planar fluid–solid interface. The objective is to verify the computational framework for predicting wave transmission and deflection at a fluid–solid interface, which is an important feature of the bubble–material interaction problem under investigation. Figure 3(a) presents the set-up of the problem. We consider a cylindrical fluid–solid domain with a diameter of 12 mm and a height of 20 mm. In the fluid subdomain, we impose a spherical pressure wave generated from a monopole source, similar to the shock wave emitted from the rapid collapse of a bubble. Specifically, we specify a Ricker wavelet, which is widely used as a model of the seismic waves from a point excitation. Table 1 shows the geometric and material information involved in the simulation.

We prescribe the Ricker wavelet as the initial condition of the fluid. Specifically, the initial pressure at a distance r from the source is given by

$$p(r) = p_0 + \frac{Q(-r/c_0)}{r}, \tag{3.1}$$

Ricker monopole source		Fluid		Solid	
f_0 (MHz)	1.43	ρ_0 (kg m^{-3})	1000	ρ_s (kg m^{-3})	1995
s_1 (μs)	0.76	p_0 (MPa)	0.101	c_L (m s^{-1})	4159
H (mm)	2.4			c_T (m s^{-1})	2319

TABLE 1. Parameters of the verification problem.
c_L: longitudinal wave speed; c_T: transverse wave speed.

with

$$Q(s) = [1 - 2\pi^2 f_0^2 (s + s_1)^2] \exp(-\pi^2 f_0^2 (s + s_1)^2), \tag{3.2}$$

where p_0 denotes the hydrostatic pressure, c_0 the speed of sound in the fluid, f_0 the frequency of Ricker wavelet and s_1 is a constant that controls the initial position of the wavelet. The values of these parameters are given in table 1. The initial velocity of the fluid is then prescribed according to the acoustic theory. The initial pressure wave has a peak magnitude of 913 Pa and a width of ∼2 mm in the radial directions (figure 3*a*). Its central peak is located at ∼1.31 mm above the material surface.

The simulation is carried out using an unstructured, finite volume fluid mesh with 21.9 million tetrahedral elements and a finite element solid mesh with 6.7 million tetrahedral elements. In the most refined region, the characteristic element size is approximately 0.01 mm for the fluid and 0.04 mm for the solid. A constant time step size of 5.0×10^{-4} μs is used in both solvers.

Figure 3(*b*) presents the numerical solution at four time instances, showing the fluid pressure field and the maximum principal stress in the solid. The simulation captures the transient dynamics of wave propagation across the fluid–solid interface, including the reflection of the pressure wave and the elastodynamic response of the solid. More specifically, figure 4 shows different types of waves that occur at a specific time instance, including the incident and the reflected waves in the fluid, the longitudinal (or *P*) and transverse (or *S*) waves in the solid, and the head waves generated by the advancing of the transmitted *P* wave along the interface.

In this problem, the maximum dynamic pressure in the fluid is two orders of magnitude smaller than the hydrostatic pressure. Therefore, the incident wave can be considered as a small disturbance and modelled as an acoustic wave propagating in a homogeneous fluid medium. Given the assumption that the solid material is isotropic and linear elastic, this problem can thus be modelled adequately by coupling the linear acoustic wave equation with the equation of motion for a linear elastic solid. The exact solution of this problem can be obtained using the Cagniard–de Hoop method (de Hoop & Van der Hijden 1984), therefore providing a reliable reference for verifying our numerical solver. We use an open-source code, Gar6more3D (INRIA 2013), to compute the exact solution. Figure 5 presents a comparison of the numerical and the analytical solutions at three sensors located in the fluid and in the solid. A close agreement is obtained. For example, the peak dynamic pressure recorded at sensor (−1.4, 1.05, 0.35) mm differs by only 0.66 % between the numerical and the analytical solutions.

3.2. *Collapse of a spherical bubble in an infinite medium*

To demonstrate the numerical model's capability of capturing single bubble dynamics, we simulate the collapse of a spherical bubble in an infinite liquid medium. The simulation

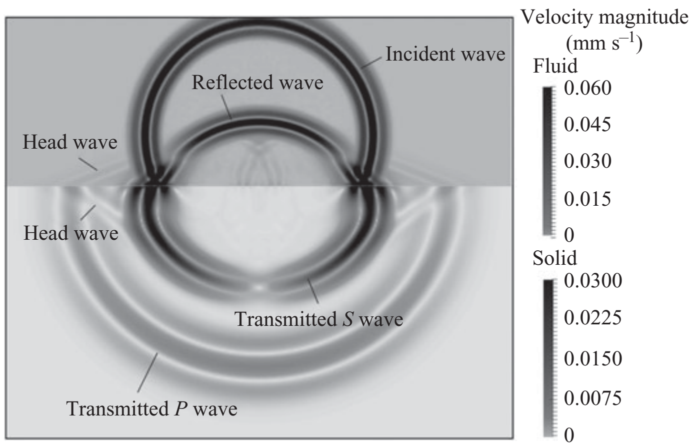

FIGURE 4. Velocity field at $t = 3\ \mu s$. The incident and reflected waves in the fluid, the transmitted waves in the solid and the head wave generated at the interface are clearly captured.

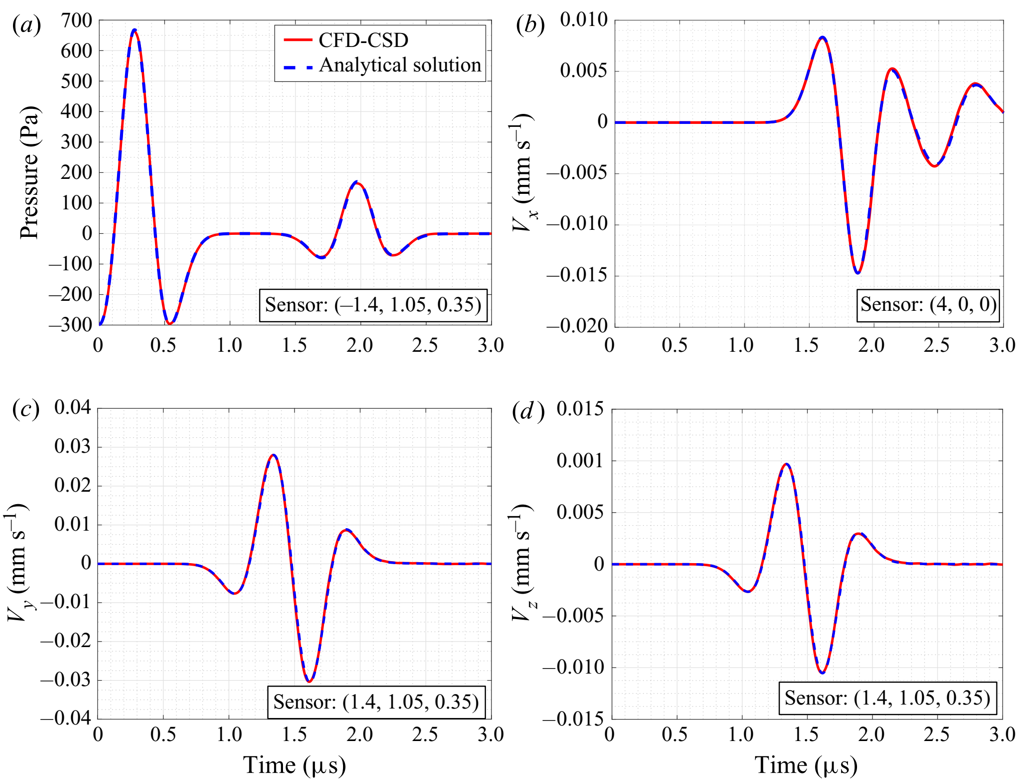

FIGURE 5. Comparison of the numerical solution obtained using the CFD (computational fluid dynamics) – CSD (computational solid dynamics) coupled solver with the analytical solution. (*a*) Time history of pressure at sensor (−1.4, 1.05, 0.35) mm in the fluid. (*b*–*d*) Time history of velocity at sensors (4, 0, 0) mm and (1.4, 1.05, 0.35) mm in the solid.

is based on the experiment of Kröninger *et al.* (2010) in which the dynamics of a laser-generated spherical bubble in water is captured using high-speed photography. We focus on simulating the initial collapse of the bubble from its maximum radius $R_0 = 0.747$ mm. We assume that when the bubble is at its maximum size, velocity is zero both inside and outside of the bubble, and the thermodynamic variables have constant values within each subdomain. Specifically, the initial density and pressure of liquid water are set to 1000 kg m^{-3} and 0.101 MPa, respectively; and the stiffened equation of state described in § 2.1 is applied. The composition and state of the gas inside the bubble was not measured in the experiment. In the simulation, we set the gas material to be air, modelled using the perfect gas equation of state ((2.3)). In previous computational studies, the initial state of the bubble is often estimated via theoretical models or data fitting (e.g. Müller *et al.* 2009; Koch *et al.* 2016) due to the lack of experimental data. Although the time history of bubble radius in those studies shows good agreement with the experimental data, the initial pressure and temperature applied therein are often unrealistically small (e.g. $p_0 = 4.579$ Pa in Müller *et al.* 2009). Here, we apply the initial density calculated in Müller *et al.* (2009) (i.e. $\rho_0 = 0.957 \times 10^{-3}$ kg m^{-3}) but use a more realistic initial pressure, $p_0 = 100$ Pa. Leveraging the spherical symmetry in this problem, the computational domain is set to be a tall and slender tetrahedron whose apex coincides with the centre of the bubble, with symmetric boundary condition applied at its three side surfaces.

Five simulations are carried out using meshes of different resolutions. Specifically, the characteristic element size (Δh) within and around the region of the bubble is refined from 60 to 3.75 μm.

Figure 6 presents the time evolution of bubble radius obtained using the five meshes. Evidently, as the mesh gets refined, the numerical result converges gradually to the experimental data for the period of bubble collapse. Figure 7 presents the velocity magnitude and the pressure field around bubble at four time instances for the converged solution. Driven by pressure difference, the bubble interface accelerates toward its interior and remains spherical during the collapse. When the bubble reaches its minimum volume, a strong shock wave is emitted.

It is noteworthy that for the time period of the bubble's rebound, the converged numerical result does not closely match the experimental data. This is likely due to the fact that the numerical model does not account for some physical processes (e.g. liquid/gas phase change) that become important when the bubble is at its minimum volume, as well as the inconsistent modelling of the bubble content (c.f. Koch *et al.* 2016). However, since the main focus of this work is the initial collapse of the bubble, the agreement with the experimental data presented above provides support for the validity of the numerical model.

4. Shock-induced bubble collapse near three representative materials

4.1. *Set-up of numerical experiment*

In this section, we consider shock-induced bubble collapse near three representative materials, namely a strengthened gypsum (BegoStone 15 : 3, Esch *et al.* 2010; Simmons *et al.* 2010), an elastomer (polyurea P1000, Amirkhizi *et al.* 2006; Chahine & Hsiao 2015) and a foam rubber (Rubatex R8702 styrene-butadiene rubber (SBR) foam, Deigan 2007). Table 2 summarizes the main properties of these materials. In particular, the relative acoustic impedance of the material compared to that of the ambient fluid (i.e. Z/Z_0) varies from 5.2 in the case of BegoStone to 1.1 in the case of polyurea and 0.2 in the case of the foam. Both polyurea and the SBR foam are modelled as a viscoelastic material.

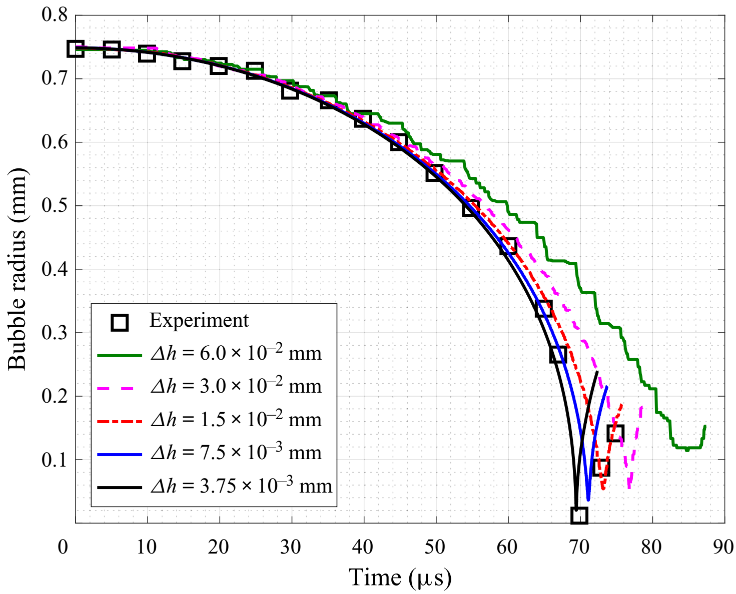

FIGURE 6. Comparison between numerical results and experimental data for the time history of bubble radius. Five sets of numerical result obtained with different mesh resolutions (Δh) are presented (the radius is calculated based on the volume of the gas domain). The experimental data are extracted from Kröninger *et al.* (2010).

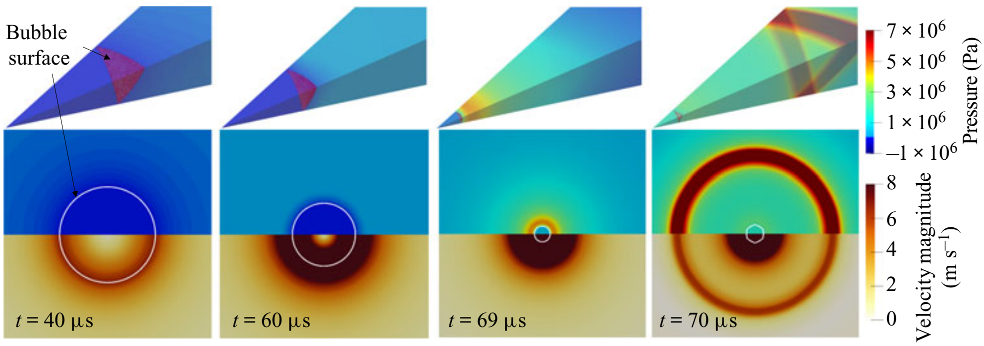

FIGURE 7. Converged solution at four time instances during collapse. Upper figure: pressure field in the tetrahedron computational domain. Lower figure: pressure and velocity magnitude in a 2-D plane across the bubble centre (the white curve represents the bubble surface). The full solution field is reconstructed by post-processing (reflection) the solution field on a plane across the apex of the tetrahedron domain.

For the BegoStone, viscoelastic effects are negligible within the small time frame considered in this study, therefore it is modelled as a purely elastic material. As a reference, we also simulate the same bubble collapsing near a rigid wall, which can be considered as a material with infinite acoustic impedance.

Figure 8 shows the set-up of the numerical experiment. Initially, a spherical air bubble with a radius of $R_0 = 0.05$ mm is placed in the liquid, at a distance of $D_0 = 2R_0$ from the material surface (measured from the centre of the bubble). The incident shock wave

Material	Density ρ_s (kg m^{-3})	Young's modulus E_0 (GPa)	Poisson's ratio ν	g_i	τ_i (μs)	Acoustic impedance Z (MPa·s m^{-1})	Z/Z_0
BegoStone	1995	27.4	0.27	—	—	8.3	5.2
Polyurea	1100	0.235	0.485	0.478	64.1	1.73	1.1
SBR foam	490	0.1586	0.3	0.37	0.01	0.32	0.2
				0.18	1.0		

TABLE 2. Material properties of three representative materials.

that induces the bubble's collapse is adopted from Johnsen & Colonius (2008). It has a compressive front with a positive peak of 35 MPa, followed by a tensile phase with a negative peak of 10.1 MPa (figure 8). This type of waveform can be generated in water through electrohydraulic or electromagnetic mechanisms (e.g. Church 1989; Fovargue *et al.* 2013). We prescribe the incident shock wave as the initial condition of the fluid governing equations, following the method described in Cao *et al.* (2019). Away from the incident shock wave, the ambient flow velocity and hydrostatic pressure are set to $v_0 = 0$ mm s^{-1} and $p_0 = 0.101$ MPa, respectively. The 3-D model described in § 2.1 is applied. Notably, this problem can also be simulated using a 2-D axisymmetric model, which may be computationally less expensive. Nonetheless, the 3-D model can be easily extended in future to investigate more complicated cases without rotational symmetry, such as problems involving multi-bubble interaction and misalignment between the shock wave and the bubble. For computational efficiency, we consider a 45° slice of the cylindrical domain with symmetry boundary conditions applied to the two cut planes, instead of modelling the entire 3-D domain. The computational domains for the solid and the fluid are discretized using 2.3 million and 19.6 million tetrahedron elements, respectively. The meshes are refined within a region close to the bubble and the fluid–solid interface, where the characteristic element size is $\Delta h_f = 1.5$ μm for the fluid mesh and $\Delta h_s = 3$ μm for the solid mesh. For comparison, the compressive front of the incident shock wave is approximately 700 μm in the liquid.

4.2. *Result and discussion*

First, a mesh convergence analysis is performed for the case of BegoStone. Four sets of mesh, including the baseline mesh introduced in § 4.1, are tested. Within the region close to the bubble, the fluid element size (Δh_f) varies from 6.0 to 0.75 μm and the solid element size (Δh_s) varies accordingly from 12.0 to 1.5 μm. Figure 9 presents the time history of relative bubble volume obtained with the four sets of mesh, showing the convergence of the results. The bubble's collapse time obtained with the finest mesh and the baseline mesh differ by less than 3 %.

Figure 10 presents four solution snapshots from the case of BegoStone. Several key features are clearly captured. The impact of the incident shock wave at the proximal (left) side of the bubble triggers the bubble's collapse. When the bubble reaches its minimum volume, a shock wave is generated. Also, during the non-spherical bubble collapse, a liquid jet forms and penetrates the bubble. These features are consistent with the results of several previous studies that considered bubble collapse near a rigid wall (e.g. Johnsen & Colonius 2008; Kobayashi *et al.* 2011). A remarkable feature of the current result is that it captures

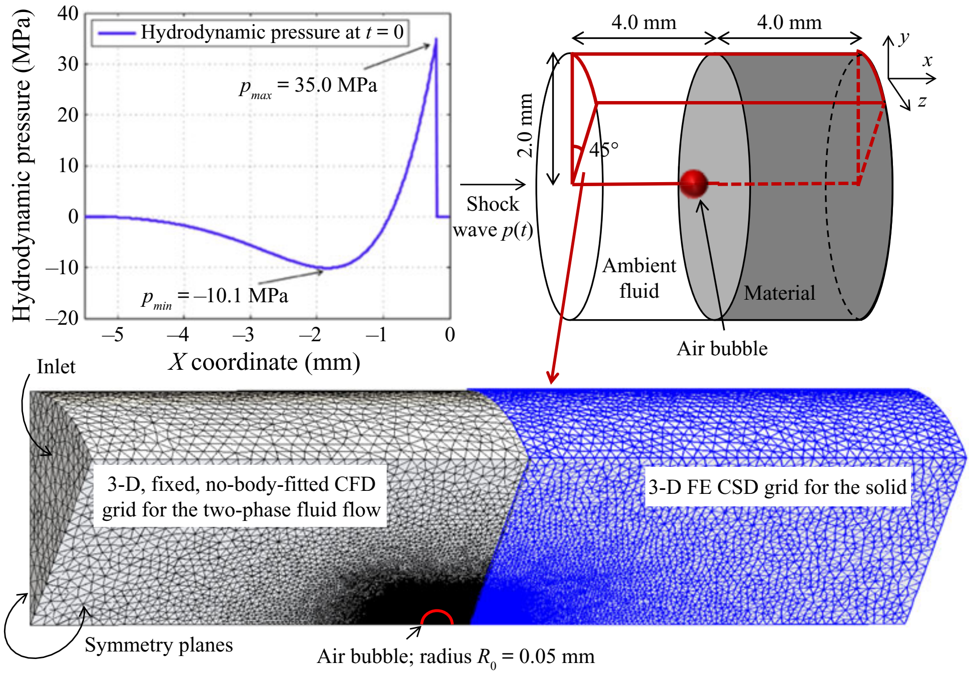

FIGURE 8. Set-up of numerical experiment. A shock wave with a magnitude of 35 MPa is applied to trigger the collapse of an air bubble with radius $R_0 = 0.05$ mm located at $D_0 = 2R_0$ from the material surface. Computations are performed on a 45° slice of the cylindrical fluid–solid domain.

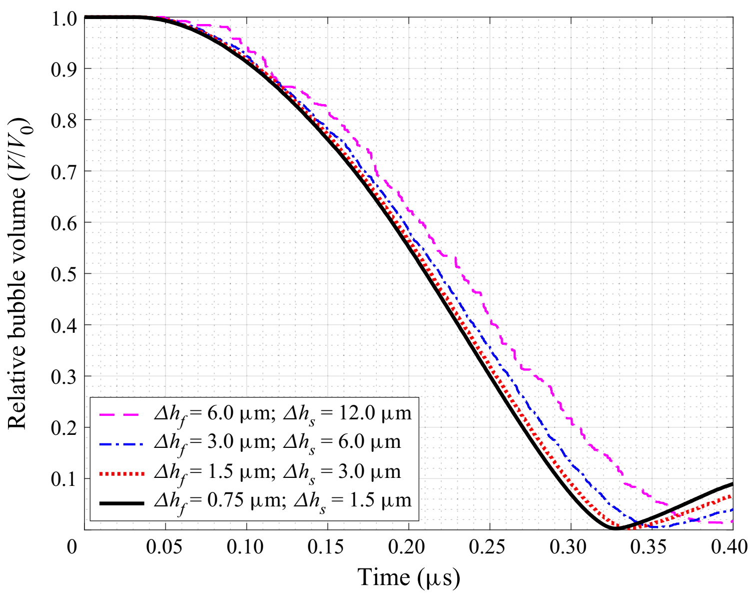

FIGURE 9. Mesh convergence analysis: time history of bubble volume obtained using four sets of mesh with refined characteristic element size (Δh) within the region close to the bubble.

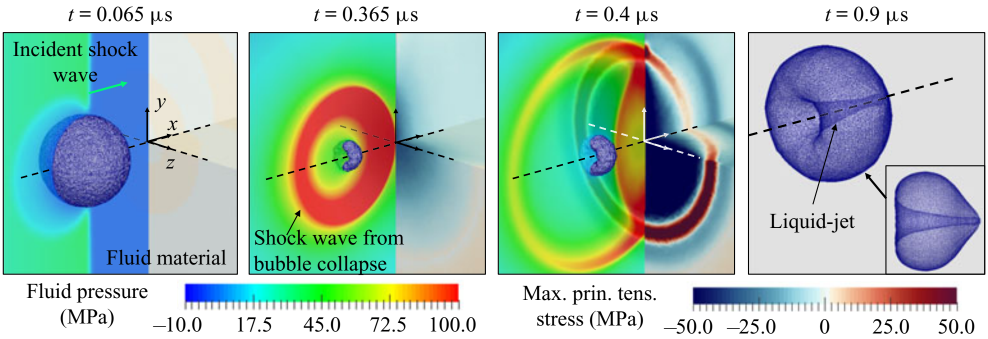

FIGURE 10. Shock-induced bubble collapse near BegoStone: transient fluid pressure, maximum principal stress inside the material and on its surface and the deformation of the bubble. The bubble's surface is captured by the 0 level set of the distance function $\phi(\boldsymbol{x}, t)$.

the transmission and reflection of the shock waves at the fluid–solid interface, as well as the resulting elastic waves inside the material.

When the same bubble collapses near different materials, the dynamics of the bubble, the fluid flow, the pressure on the material surface and the stress inside the material all vary. Figure 11 provides a comparison of the three cases by showing the fluid pressure field and the maximum principal stress inside the solid at six time instances. The first major difference lies in the reflection of the incident shock wave at the material surface. This can be observed from the second row of images in figure 11, which are taken at $t = 0.155$ μs, when the reflection has just reached the distal (right) side of the bubble. In the case of BegoStone, the reflected wave is compressive, with peak pressure around 23 MPa. In the case of polyurea, the reflected wave is also compressive, but its amplitude is only ∼2 MPa. By contrast, the reflection is a tensile wave in the case of the foam, with peak pressure around −25 MPa. At the same time, a fraction of the incident wave is transmitted into the material as a compressive stress wave. Figure 11 shows that both the amplitude and the propagation speed of the wave vary from case to case. The peak value of the maximum principal stress is found to be around −57 MPa (compressive) for BegoStone, −35 MPa for polyurea and −10 MPa for the foam.

The differences described above can be explained by the relative acoustic impedance of each material compared to that of the ambient fluid (i.e. Z/Z_0). Consider a simplified one-dimensional problem in which an incident wave with amplitude p_i impinges on a surface in its normal direction. According to the acoustic wave theory Brekhovskikh & Godin 2012), the amplitude of the reflected and transmitted waves, p_r and p_t, are given by

$$p_r = p_i \frac{Z/Z_0 - 1}{Z/Z_0 + 1}, \tag{4.1}$$

and

$$p_t = p_i \frac{2Z/Z_0}{Z/Z_0 + 1}, \tag{4.2}$$

respectively. For $p_i = 35.0$ MPa (peak pressure of the incident shock wave), we obtain $p_r = 23.7$ MPa and $p_t = 58.7$ MPa for BegoStone, $p_r = 1.4$ MPa and $p_t = 36.4$ MPa for polyurea, and $p_r = -23.3$ MPa and $p_t = 11.7$ MPa for the foam. These values match reasonably well with the aforementioned results of the three-dimensional simulations.

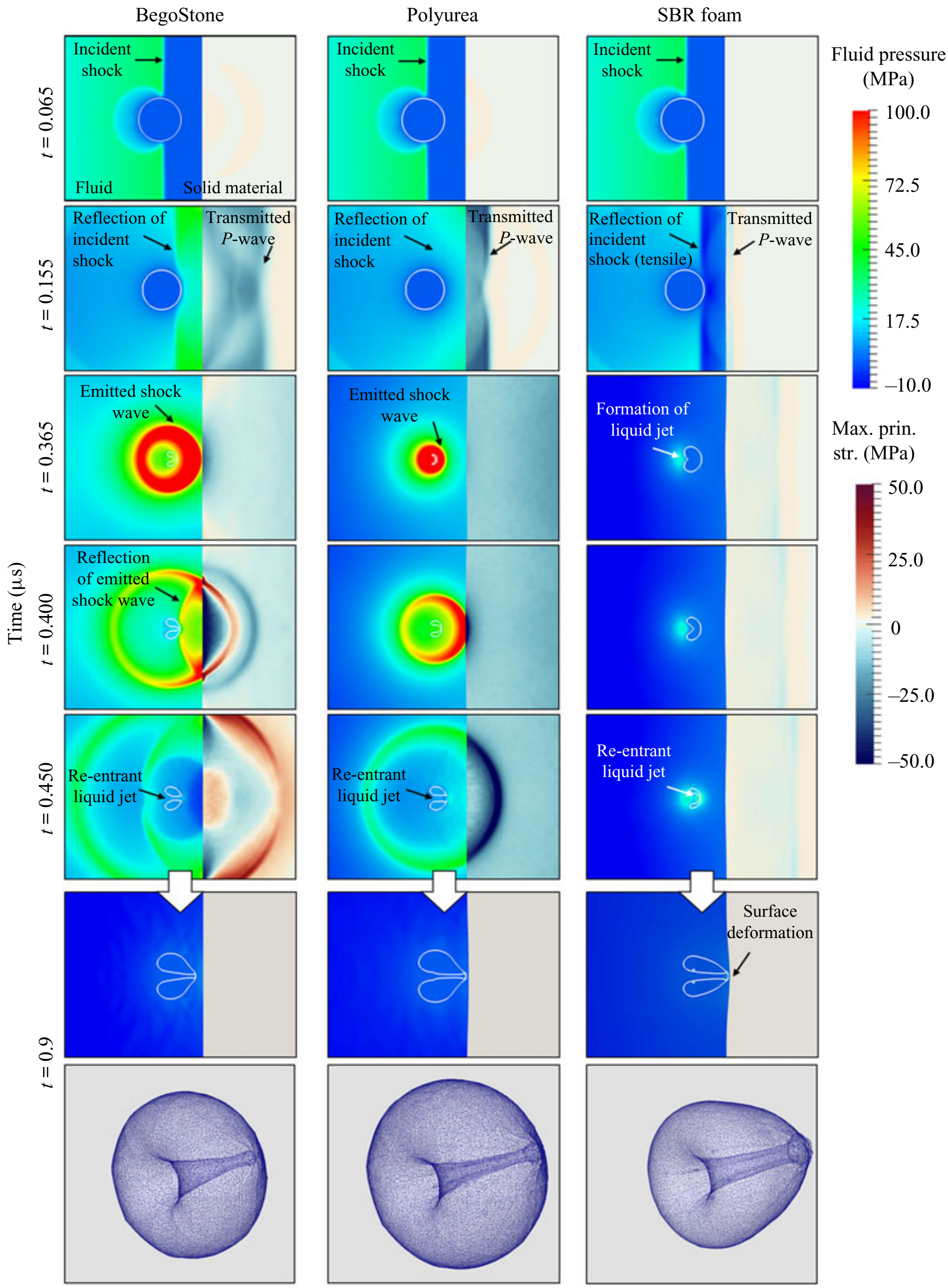

FIGURE 11. Shock-induced bubble collapse near three different materials: fluid pressure and maximum principal stress.

In all the three cases, the reflected wave impinges on the bubble from the distal (right) side at a time it just started to collapse (cf. the second row of images in figure 11). In the case of BegoStone, the reflected wave is compressive, with an amplitude comparable to that of the incident shock. Therefore it accelerates the bubble's collapse. By contrast, the reflected wave in the case of the foam creates a tensile stress field around the bubble, which slows down its collapse. The variation in the speed of collapse can be observed from the third row of images in figure 11, taken at $t = 0.365$ μs. By this time, the bubble near BegoStone had already reached its minimum volume and is rebounding. The front of the shock wave emitted from its collapse has just arrived at the material surface. At the same time, the bubble near polyurea has just reached its minimum volume. The collapse of the bubble near the foam is much slower. Its minimum volume is reached around $t = 0.5$ μs.

The variation in the speed of collapse has a clear impact on the emission of a shock wave and its magnitude, which can be observed from the images taken between $t = 0.365$ μs and $t = 0.450$ μs (i.e. the third, fourth and fifth rows of images in figure 11). A striking difference is that the emission of shock wave is observed only in the cases of BegoStone and polyurea, but not in the case of the foam. Moreover, the magnitude of the emitted shock wave is much higher in the case of BegoStone than in the case of polyurea.

When the emitted shock wave reaches the material surface, a fraction of the energy is reflected. Again, the type (i.e. compression or tension) and amplitude of the reflected wave depend on the material's acoustic impedance. When the reflected wave impinges on the bubble, it is in the process of rebound. In the case of BegoStone, this instance is captured by the snapshot at $t = 0.400$ μs. For a material with high acoustic impedance, the reflected wave is compressive, and its amplitude can be higher than that of the incident shock. Later we will show that the reflection of the emitted shock wave has an impact on both the speed of the bubble's rebound and the velocity of the liquid jet.

Furthermore, the images from 0.4 to 0.9 μs in figure 11 show that in all the three cases, the bubble penetrates itself while rebounding from its minimum volume, thereby generating a liquid jet that moves towards the material surface. In the case of the foam, this liquid jet creates a dimple on the material surface, which can be observed from the image at $t = 0.9$ μs in figure 11. In the other two cases, the deformation is smaller due to the stiffness of the materials.

Next, we take a closer look at the fluid dynamics by examining the time history of bubble volume, the shock wave emitted at the end of bubble collapse and the fluid velocity field.

Figure 12 compares the time history of bubble volume for all the simulated cases, including the degenerate case of the same bubble collapsing near a rigid wall. The bubble's volume is initially the same in all the cases, until approximately 0.15 μs, when the reflection of the incident shock arrives at the distal side of the bubble. Afterwards, the four curves in figure 12 start to diverge, indicating a clear impact of the reflected wave. The bubble's collapse time, defined as the time between the arrival of the incident shock wave and the time the bubble reaches its minimum volume, increases from 0.293 μs in the case of rigid wall to 0.306 μs in the case of BegoStone, 0.335 μs in the case of polyurea, and 0.465 μs in the case of the foam. Also, the bubble's minimum relative volume increases in the same order from 2.4×10^{-3} in the case of the rigid wall to 4.7×10^{-2} in the case of the foam. Given the causal relation between the material's acoustic impedance and the type (compression or tension) and amplitude of the reflected wave, the result shown in figure 12 suggests that in the current context, a solid material with lower acoustic impedance may reduce both the energy released from bubble collapse and its peak power.

When the cases of rigid wall, BegoStone, and polyurea are compared, it is interesting to note that the speed of the bubble's rebound has the opposite trend compared to that of the collapse. Specifically, the time it takes for the bubble to rebound from its minimum volume to 1/5 of its initial volume decreases from 0.38 μs in the case of rigid wall to 0.24 μs in the case of BegoStone and 0.14 μs in the case of polyurea. This trend reversal can be attributed to the reflection of the shock wave resulting from bubble collapse (i.e. the

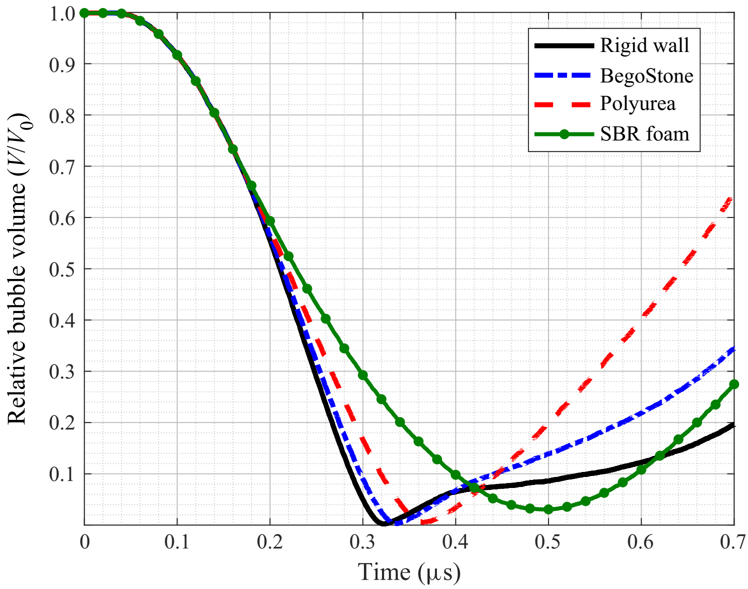

FIGURE 12. Comparison of the time history of bubble volume with different solid and soft materials in its vicinity.

Material	Z/Z_0	Bubble's minimum relative volume	Bubble's collapse time (μs)	Peak surface pressure (MPa)
Rigid wall	∞	2.4×10^{-3}	0.293	341
BegoStone	5.2	2.8×10^{-3}	0.306	255
Polyurea	1.1	5.4×10^{-3}	0.335	119
SBR foam	0.2	4.7×10^{-2}	0.465	No shock wave

TABLE 3. Comparison of the dynamics of bubble collapse near rigid wall, BegoStone, polyurea and SBR foam.

emitted shock wave) at the material surface. A material with higher acoustic impedance sends back a stronger compressive wave, which leads to slower bubble rebound.

Figure 13 shows the time history of hydrodynamic pressure at the centre of the material surface. The peak pressure of the shock wave emitted from bubble collapse is 341 MPa in the case of rigid wall (which agrees reasonably well with the previous study of Johnsen & Colonius 2008), 255 MPa in the case of BegoStone, and 119 MPa in the case of polyurea. As expected, it correlates positively with the speed of bubble collapse (cf. figure 12). In all these three cases, the peak pressure value is significantly higher than the amplitude of the incident shock wave, which is 35 MPa. In the case of the foam, the bubble's collapse does not generate a shock wave. Therefore, compared to the other cases, the time history of sensor pressure in the case of the foam is nearly a flat line. The impulse of dynamic pressure at the sensor location is found to be 13.5, 11.5, 8.0 and 1.5 MPa-μs in the case of the rigid wall, BegoStone, polyurea and the foam, respectively.

For ease of comparison, table 3 summarizes the bubble's minimum volume, collapse time and the peak surface pressure induced by the emitted shock wave in all four cases.

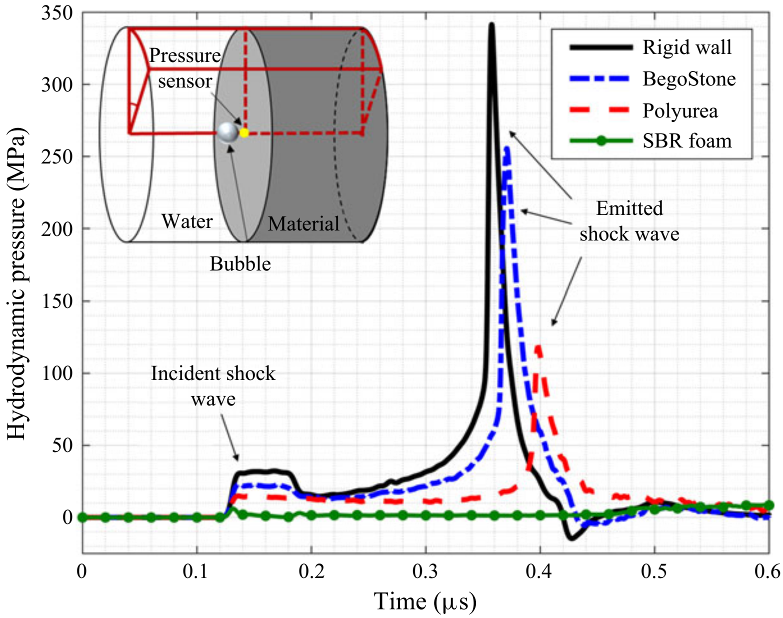

FIGURE 13. Time history of hydrodynamic pressure at a sensor on the material surface. The magnitude of the emitted shock wave becomes smaller as the material's acoustic impedance decreases. No shock wave is observed in the case of SBR foam.

The evolution of the fluid velocity field also varies from case to case. Figure 14 shows the velocity field around the bubble during its collapse and rebound. The first row of images are taken shortly after the reflection of the incident shock passes through the bubble. Comparing the three cases shown in the figure, a variation of the speed of collapse can be observed. To clarify the difference, figure 15 compares the time history of x-velocity at the proximal and distal sides of the bubble for the three materials. In the case of BegoStone, the velocity difference between the proximal and distal sides of the bubble reaches 1600 m s^{-1} shortly before contact. This is 1.6 times higher than the maximum velocity observed in the case of polyurea, and 4 times higher than that for the foam.

Figure 14 also shows the formation and evolution of the liquid jet. Comparing the three cases presented in the figure, it is notable that there is not a positive correlation between the velocity of the liquid jet and the speed of the bubble's collapse. In particular, after $t = 0.4$ μs, the velocity of the jet is lower in the case of BegoStone than in the case of polyurea, despite that in the former case the bubble collapsed faster. This phenomenon is due to the reflection of the emitted shock wave at the material surface, and is essentially an effect of the material's acoustic impedance. More specifically, because of a higher acoustic impedance, BegoStone reflects a larger fraction of the incident shock wave back to the bubble (cf. figure 11, $t = 0.155$ μs), which accelerates the bubble's collapse, therefore emitting a stronger shock wave at the end of the collapse (cf. figure 13). For the same reason, BegoStone sends back a stronger (compressive) reflected wave when the emitted shock wave reaches the material surface. This reflection arrives at the distal side of the bubble at $t = 0.4$ μs, when the liquid jet has just formed (figures 11 and 14). Thus the velocity of the jet is reduced due to the impact of the reflected wave. In the case of the foam, the collapse of the bubble is decelerated by the reflection of the incident wave (which is tensile, due to the material's low acoustic impedance). Therefore, as the liquid

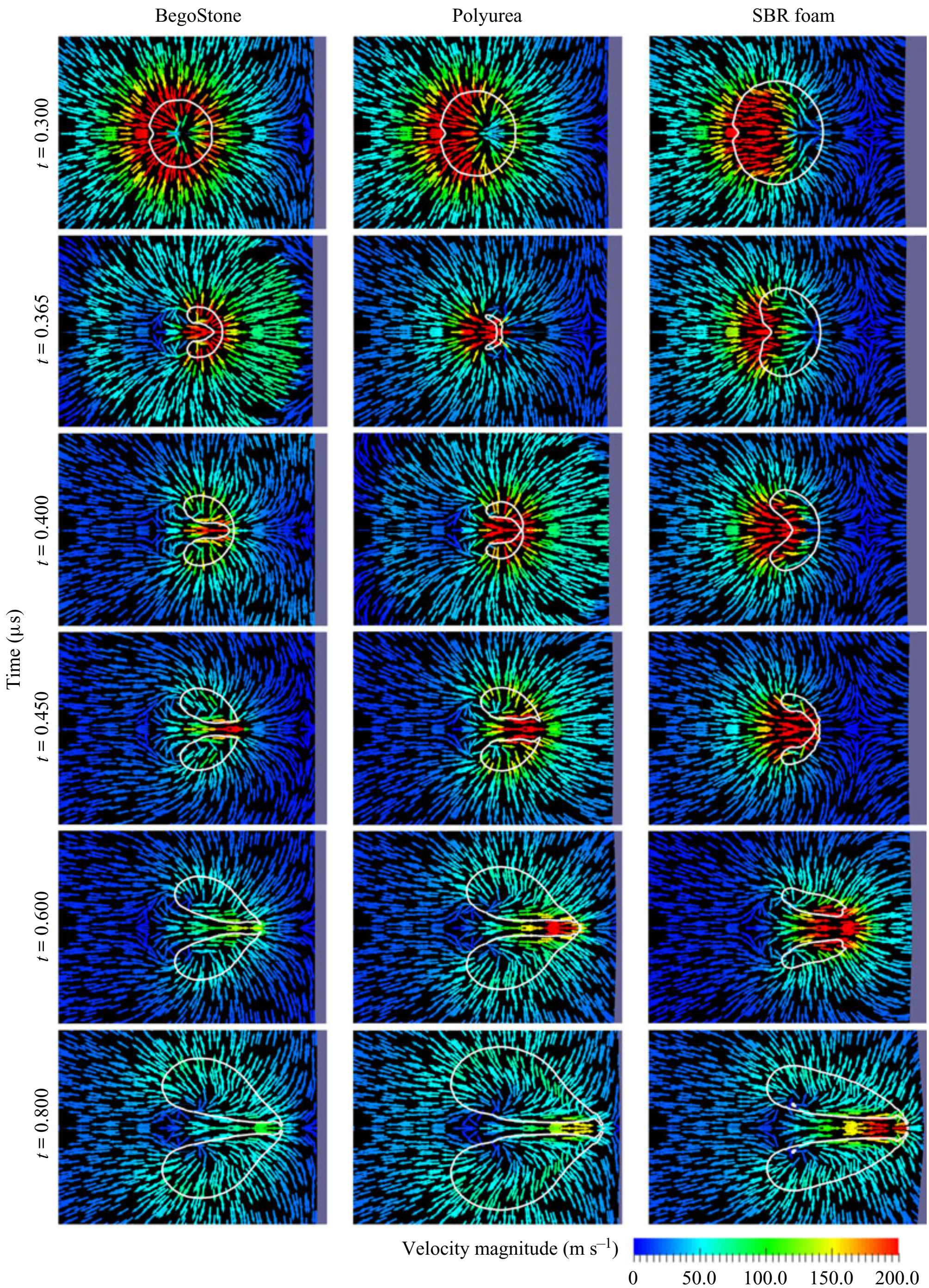

FIGURE 14. Comparison of the evolution of fluid velocity during bubble collapse and rebound, with different materials in the vicinity. Snapshots at six time instances are compared. Three supplementary movies showing the full evolution for the case of BegoStone (movie 1), Polyurea (movie 2) and SBR foam (movie 3) are available online at https://doi.org/10.1017/jfm.2020.810.

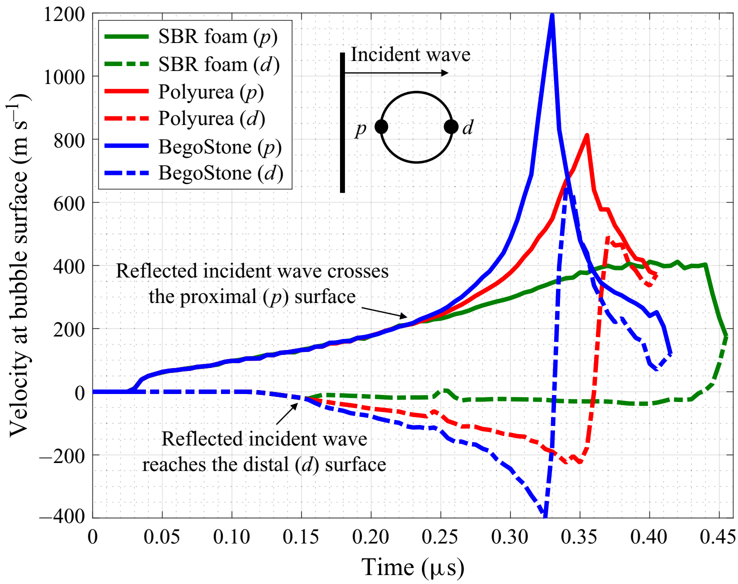

FIGURE 15. Time history of fluid velocity on the proximal (p) and distal (d) sides of the bubble surface.

jet approaches the material surface, its velocity is higher than both of the other two cases (see the last two rows of images in figure 14). This chain reaction highlights an interaction of bubble, fluid and solid dynamics, and can be summarized by a sequence of events as below.

(*a*) When the incident shock wave arrives, because of the difference in acoustic impedance, BegoStone reflects a strong compressive wave to the bubble, while the foam sends back a tensile wave (figure 11, $t = 0.155$ μs).

(*b*) Because of (*a*), the bubble in the case of BegoStone collapses much faster than the bubble in the case of the foam (figures 11 and 14, $t \leq 0.365$ μs for BegoStone, and $t \leq 0.45$ μs for the foam).

(*c*) Because of (*b*), the bubble in the case of BegoStone emits a strong shock wave at the end of its collapse (figure 11, $t \leq 0.365$ μs), which is absent in the case of the foam (figure 11, $t \leq 0.45$ μs).

(*d*) Because of (*c*), BegoStone sends back another compressive wave towards the bubble when the emitted shock wave arrives at its surface (figure 11, 0.365 μs $\leq t \leq 0.4$ μs). This event does not occur in the case of the foam.

(*e*) Because of (*d*), the liquid jet in the case of BegoStone is decelerated (figure 14, 0.4 μs $\leq t \leq 0.8$ μs).

(*f*) Because of (*e*), the jet velocity at the material surface is much lower in the case of BegoStone than in the case of the foam (figure 14, $t = 0.8$ μs).

The transient stress field inside the solid material also varies from case to case. For example, figures 16(*a*) and 16(*b*) show the response of BegoStone and polyurea to the shock wave emitted from bubble collapse. For both materials, a longitudinal wave (P-wave) and a transverse wave (S-wave) are captured. For BegoStone, the speeds of longitudinal and transverse waves are 4159 m s^{-1} and 2319 m s^{-1}, greater than the

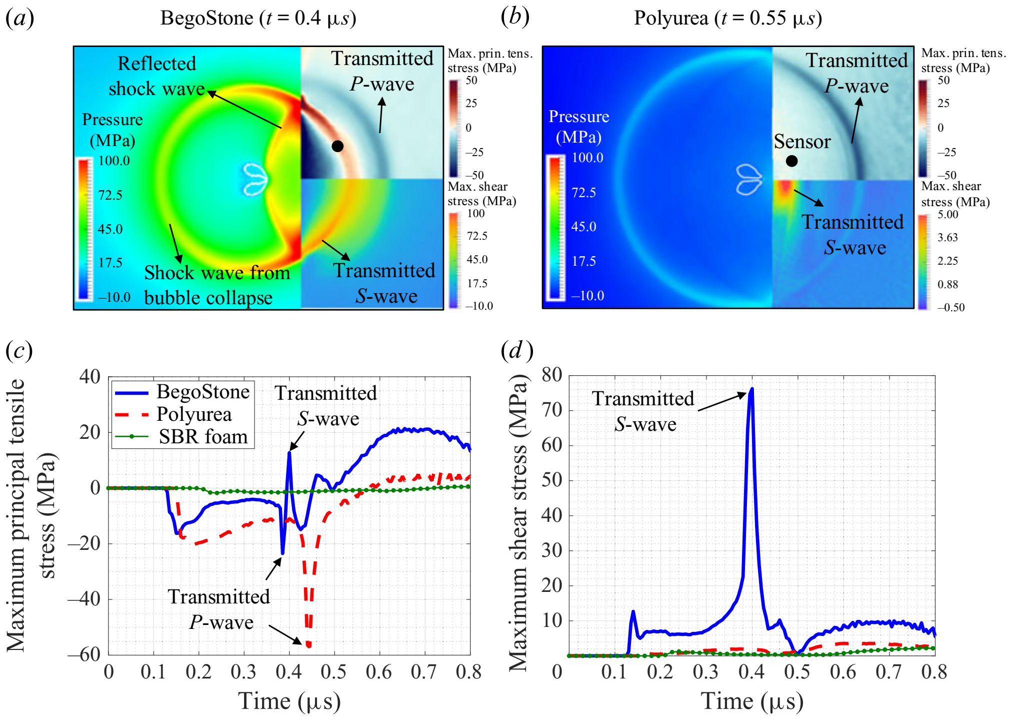

FIGURE 16. (*a*,*b*) Two snapshots showing different elastic waves propagating in BegoStone and the polyurea. (*c*,*d*) Time history of the maximum principal tensile stress and the maximum shear stress at a sensor located at (0.05, 0.05, 0.0) mm.

speed of sound in water. Therefore, in figure 16(*a*) both waves have a crescent shape, and the longitudinal wave is clearly forward of the shock wave in water. In polyurea, the longitudinal wave travels at a speed of 1600 m s^{-1}, which is close to the speed of sound in water. Hence in figure 16(*b*) the front of the longitudinal wave is almost aligned with the shock front at the fluid–solid interface. Also, the transverse wave in polyurea is roughly parallel to the fluid–solid interface. This is because the speed of transverse waves in polyurea is around 300 m s^{-1}, much smaller than the speed of sound in water. In addition, figure 16(*c*,*d*) compares the time history of maximum principal tensile stress and maximum shear stress at a sensor, which also show clear differences among the three materials.

Remark: In combination, the results of fluid pressure (figures 11 and 13) and velocity (figure 14) suggest that under the simulated condition, the primary mechanism of material damage may depend upon the material's acoustic impedance. For a 'hard' material with relatively high acoustic impedance, the primary mechanism may be the shock wave emitted at the end of the bubble collapse. For a 'soft' material with relatively low acoustic impedance, the primary mechanism appears to be the liquid jet. This finding is generally consistent with the results of some previous studies, such as Tomita & Shima (1986), Shaw *et al.* (2000), Sankin & Zhong (2006) and Abouel-Kasem *et al.* (2009), although the material and condition considered in each study are different.

Material	Acoustic impedance Z (MPa·s m^{-1})	Density ρ_s (kg m^{-3})	Young's modulus E (GPa)	Poisson's ratio ν
M1 (BegoStone)	8.3	1995	27.4	0.27
M2	8.3	1995	13.7	0.418
M3	8.3	1995	6.85	0.463
M4	8.3	1995	1.71	0.491

TABLE 4. Test 1 material properties.

5. Parametric study on the effects of acoustic impedance

5.1. *Acoustic impedance as a key parameter*

The results presented in § 4 show that the acoustic impedance of the solid material has significant impact on the bubble and fluid dynamics. A complexity, however, is that acoustic impedance is a function of the material's density and elastic properties. Specifically (see, e.g. Brekhovskikh & Godin 2012),

$$Z = \sqrt{\frac{\rho_s E(1-\nu)}{(1+\nu)(1-2\nu)}}. \tag{5.1}$$

Therefore, it is impossible to vary acoustic impedance while keeping all the other properties the same, or to fix acoustic impedance while varying only one of the other properties. Indeed, because the materials considered in § 4 are selected from real-world materials of practical importance, they differ not only in Z, but also in ρ_s, E and ν.

To gain more insight into the role of acoustic impedance, we consider three numerical tests that involve artificial materials with prescribed properties. In each test, we fix the value of Z, and vary two of the three parameters: ρ_s, E and ν.

(i) Test 1: shock-induced bubble collapse near a series of materials that have the same values of Z and ρ_s, but different values of E and ν.
(ii) Test 2: shock-induced bubble collapse near a series of materials that have the same values of Z and ν, but different values of ρ_s and E.
(iii) Test 3: shock-induced bubble collapse near a series of materials that have the same values of Z and E, but different values of ρ_s and ν.

In Test 1, we consider four materials as shown in table 4, including BegoStone. Their Young's modulus and Poisson's ratio vary by a factor of 16 and 1.8, respectively. For each material, we perform the numerical analysis described in § 4.1, using the same computational model.

Table 5 summarizes the results obtained from Test 1, including the bubble's collapse time (t_c), the minimum bubble volume (V_{min}/V_0), the maximum pressure at the sensor shown in figure 13 and the maximum values of maximum principal and shear stresses at the sensor shown in figure 16. The table shows that when Z and ρ_s are fixed, the bubble and fluid dynamics are relatively insensitive to variation in E or ν. The small changes can be explained by the fact that while the material's density and longitudinal wave speed are fixed, the transverse wave speed does vary among the four materials. For the same reason, it is not surprising that the stress field inside the material clearly varies among the four cases.

Material	Bubble's collapse time t_c (μs)	Minimum bubble volume V_{min}/V_0	Max. pressure at sensor (MPa)	MPS (MPa)	MSS (MPa)
M1	0.31	0.003	255	−23.5	76
M2	0.31	0.003	250	−75.2	47
M3	0.30	0.003	250	−96.1	30
M4	0.30	0.003	242	−96.2	12

TABLE 5. Test 1 results.
MPS and MSS: the temporal maximum of maximum principal stress and maximum shear stress at the sensor shown in figure 16. For MPS, the negative (i.e. compressive) peak is shown.

Material	Acoustic impedance Z (MPa·s m^{-1})	Density ρ_s (kg m^{-3})	Young's modulus E_0 (GPa)	Poisson's ratio ν
M5	17.28	1500	134.4	0.33
M6 (Al7075)	17.28	2810	71.7	0.33
M7	17.28	5000	40.3	0.33
M8	17.28	10 000	20.2	0.33

TABLE 6. Test 2 material properties.

Material	Acoustic impedance Z (MPa·s m^{-1})	Density ρ_s (kg m^{-3})	Young's modulus E (GPa)	Poisson's ratio ν
M9	1.73	733	0.235	0.490134
M10 (Polyurea)	1.73	1100	0.235	0.485
M11	1.73	2200	0.235	0.46871
M12	1.73	5500	0.235	0.40937

TABLE 7. Test 3 material properties.

In the same way, we perform Test 2 for the materials shown in table 6, in which ρ_s varies from 1500 to 10 000 kg m^{-3}, and E from 20.2 to 134.4 GPa. The result shows that t_c varies by less than 1 %, from 0.298 to 0.300 μs; V_{min}/V_0 varies by around 3 %, from 0.00275 to 0.00285. The maximum sensor pressure varies by around 5 %, from 280 to 296 MPa. In comparison, variation in the material's stress field is much larger. For example, at the aforementioned sensor location (figure 16), the peak value of maximum shear stress varies from 121.4 to 200.1 MPa.

In Test 3, we consider the four materials shown in table 7. The material's acoustic impedance and Young's modulus are fixed, and their density and Poisson's ratio vary by a factor of 7.5 and 1.2, respectively. Again, the fluid results are relatively insensitive to the material variations. For example, the peak pressure at the aforementioned sensor location varies by ∼5 %, from 119 to 125 MPa.

Combining the results of the above numerical tests and those presented in § 4, it is evident that under the simulated conditions, the solid material's acoustic impedance (Z) is an important parameter that controls the material's reciprocal effect to the two-phase fluid flow. The same bubble collapsing near materials with different values of Z can produce

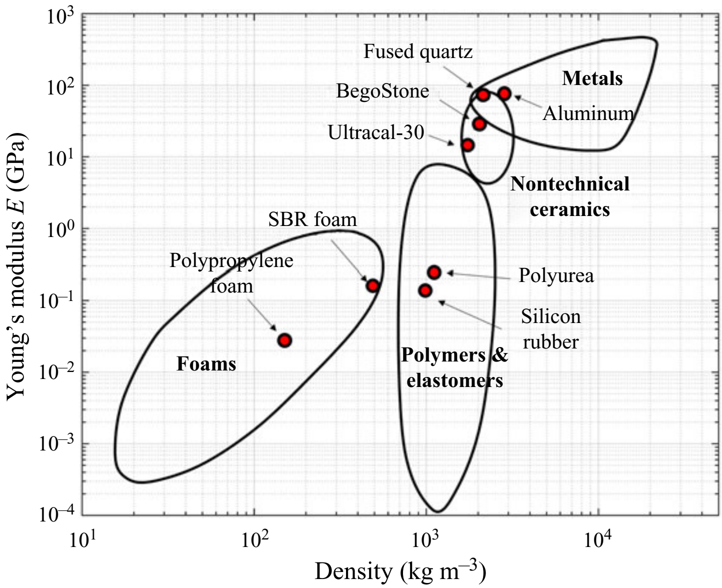

FIGURE 17. Selected materials for parametric study (the Young's modulus–density diagram is adapted from Ashby 2010).

Material	Acoustic impedance Z (MPa·s m^{-1})	Z/Z_0	Density ρ_s (kg m^{-3})	Young's modulus E (GPa)	Poisson's ratio ν
Aluminium 7075	17.28	10.8	2810	71.7	0.33
Fused Quartz (GE Type 214)	13	8.1	2200	72	0.17
U-30 artificial stone (Esch *et al.* 2010)	5.38	3.4	1693	14.7	0.231
Silicone rubber (Folds 1974)	1.06	0.66	990	0.13	0.48
Polypropylene foam (Bouix, *et al.* 2009)	0.063	0.04	150	0.027	0.01

TABLE 8. Properties of five additional materials with different acoustic impedance.

clearly different bubble and fluid dynamics, with $Z = Z_0$ being a transition point. On the other hand, the same bubble collapsing near materials that have the same value of Z, yet differ in other elastic properties, are found to produce similar bubble and fluid dynamics (yet dissimilar stress field inside the material).

5.2. *Selection of materials with different values of acoustic impedance*

To characterize the effect of acoustic impedance on bubble and fluid dynamics, we select five additional materials with acoustic impedance varying in a broader range compared to those considered in § 4. The materials are selected from several broad categories, as shown in figure 17. Table 8 summarizes the properties of these materials. In particular, their acoustic impedance varies from 0.063 to 17.28 MPa·s m^{-1}. For each material, we conduct the same numerical analysis described in § 4.1.

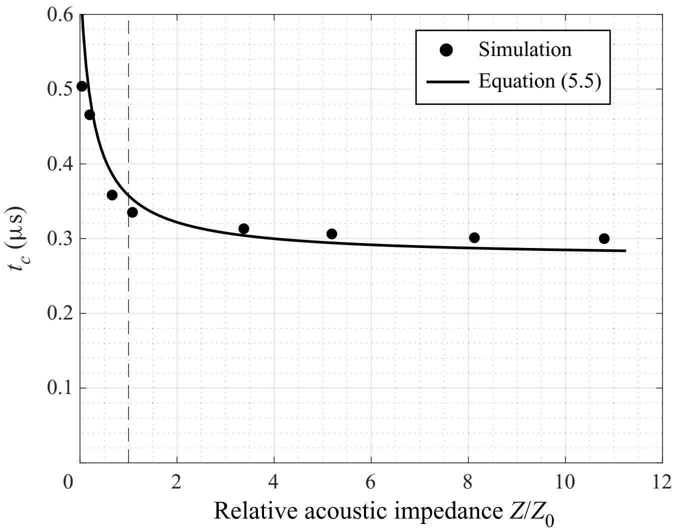

FIGURE 18. Effect of material's acoustic impedance on the bubble's collapse time. Dashed line: $Z = Z_0$.

In the following, we combine the new materials in table 8 with those considered in § 4 (table 2), and characterize the effect of acoustic impedance on three fluid quantities of interest, namely the bubble's collapse time, the minimum bubble volume and the maximum hydrodynamic pressure on the material surface.

5.3. *Effect of acoustic impedance on bubble collapse time*

Figure 18 shows in black dots the bubble's collapse time, t_c, for the eight materials considered. As the material's acoustic impedance increases, t_c decreases monotonically. This trend is consistent with what we found in § 4 using the three representative materials, and has been explained there. The dashed line in figure 18 marks $Z/Z_0 = 1$. For materials with $Z/Z_0 > 1$, the variation in t_c is relatively small. For example, as Z/Z_0 decreases from 10.8 (aluminium) to 1.1 (polyurea), t_c increases by 10 %. When $Z/Z_0 < 1$, t_c becomes more sensitive to Z. It increases from 0.36 μs in the case of the rubber ($Z/Z_0 = 0.66$) to 0.465 μs in the case of the SBR foam ($Z/Z_0 = 0.2$).

The trend shown in figure 18 can be captured using a simple model. We recall that in the case of free-field Rayleigh collapse modelled by the Rayleigh–Plesset equation, after neglecting the gas content inside the bubble, the collapse time can be derived as (Brennen 2014)

$$t_c^R = 0.915\sqrt{\frac{\rho_l}{p_\infty - p_v}}R_0, \tag{5.2}$$

in which the superscript R denotes Rayleigh collapse; ρ_l denotes the density of the liquid, p_∞ the far field pressure, p_v the vapor pressure and R_0 the initial bubble radius. Further, for the non-spherical Rayleigh collapse of a bubble near a rigid wall, Rattray (1951) proposed that the bubble's collapse time can be approximated by

$$t_c^{R,w} \approx t_c^R\left(1 + 0.205\frac{R_0}{D_0}\right) = 0.915\sqrt{\frac{\rho_l}{p_\infty - p_v}}R_0\left(1 + 0.205\frac{R_0}{D_0}\right), \tag{5.3}$$

where the superscript w on t_c denotes wall, and D_0 is the distance between the centre of the bubble to the wall (cf. Johnsen & Colonius 2009; Koch *et al.* 2016).

In the present study, the bubble's collapse is induced by a shock wave, which is different from a uniform pressure p_∞ in Raleigh collapse. Moreover, in § 4 we have shown that the bubble's collapse time depends sensitively on both the incident shock and its reflection against the material surface, while the amplitude of the reflected wave is a function of Z/Z_0. Therefore, we replace p_∞ in (5.3) by

$$p_s = p_i + c_r p_r = p_i\left(1 + c_r\frac{Z/Z_0 - 1}{Z/Z_0 + 1}\right), \tag{5.4}$$

where p_i is a characteristic pressure of the incident shock, p_r the pressure of its reflection ((4.1)), and c_r a non-dimensional coefficient that accounts for the time lag between the impact of the incident shock wave and that of the reflected wave. In other words, we propose that for the current study, the bubble's collapse time can be described by

$$t_c = 0.915\sqrt{\frac{\rho_l}{p_i\left(1 + c_r\dfrac{Z/Z_0 - 1}{Z/Z_0 + 1}\right) - p_v}}R_0\left(1 + 0.205\frac{R_0}{D_0}\right). \tag{5.5}$$

The solid line in figure 18 shows the prediction of the above model, with $p_i = 20$ MPa (approximately half of the peak pressure of the incident shock) and $c_r = 0.7$. It agrees well with the result of the numerical analysis.

5.4. *Effect of acoustic impedance on minimum bubble volume*

In figure 19, the black dots show the bubble's minimum volume normalized by its initial volume, i.e. V_{min}/V_0, for the eight materials considered. As the material's acoustic impedance increases, V_{min}/V_0 decreases monotonically. The trend is nonlinear and again, $Z/Z_0 = 1$ roughly marks a turning point. The minimum bubble volume is more sensitive to the nearby material's acoustic impedance when $Z/Z_0 < 1$. For example, V_{min}/V_0 in the case of polypropylene foam ($Z/Z_0 = 0.04$) is more than 9 times higher than that in the case of rubber ($Z/Z_0 = 0.66$). In comparison, the difference between the case of Ultracal-30 stone ($Z/Z_0 = 3.4$) and the case of aluminium ($Z/Z_0 = 10.8$) is less than 20 %.

The effect of acoustic impedance on minimum bubble volume can also be captured using a phenomenological model derived from the Rayleigh–Plesset equation. Again, we recall that in the case of free-field Rayleigh collapse modelled by the Rayleigh–Plesset equation, the minimum bubble volume can be derived analytically (Brennen 2014). After neglecting surface tension, we have

$$R^R_{min} = R_0\left[\frac{p_{G_0}}{(\gamma_G - 1)\,(p_\infty - p_v)}\right]^{1/[3(\gamma_G-1)]}, \tag{5.6}$$

where R^R_{min} denotes the minimum radius of the bubble, which is assumed to remain spherical all the time. Again, the superscript R denotes Rayleigh collapse; p_{G_0} denotes the partial pressure of gas inside the bubble; p_v denotes the vapor pressure; and γ_G the specific heat ratio of the internal gas.

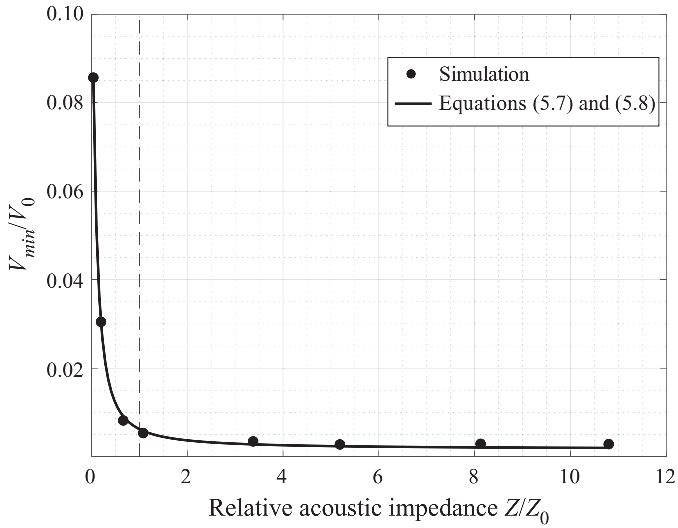

FIGURE 19. Effect of material's acoustic impedance on the bubble's minimal volume. Dashed line: $Z = Z_0$.

To account for non-spherical collapse, we generalize the definition of bubble radius (R) as

$$R = \left(\frac{V}{4\pi/3}\right)^{1/3}. \tag{5.7}$$

Then, we generalize the above analytical result from Rayleigh–Plesset equation in the same way described in § 5.3, which gives

$$R_{min} = R_0 c_s \left[\frac{p_0}{(\gamma_G - 1)\left[p_i\left(1 + c_r \dfrac{Z - Z_0}{Z + Z_0}\right) - p_v\right]}\right]^{1/[3(\gamma_G - 1)]}. \tag{5.8}$$

The solid line in figure 19 shows the minimum bubble volume predicted by (5.8) with $p_i = 20$ MPa, $c_r = 0.7$ and $c_s = 7.0$. The prediction agrees well with the result of numerical analysis.

5.5. *Effect on the maximum pressure on material surface*

Figure 20 shows in black dots the maximum hydrodynamic pressure on the material surface, denoted by $p_{w,max}$, for the eight materials considered. Again, a monotonic relationship is observed. Specifically, as Z/Z_0 varies from 0.04 (in the case of the polypropylene foam) to 10.8 (in the case of aluminium 7075), $p_{w,max}$ increases by 26 times, from 11.3 to 291.6 MPa. The increase of maximum pressure is nonlinear with respect to Z/Z_0, and the slope reduces as the acoustic impedance becomes larger (i.e. concave). It can be expected that as Z/Z_0 goes to infinity, p_{max} would approach the value obtained from the case with a rigid wall (cf. figure 13).

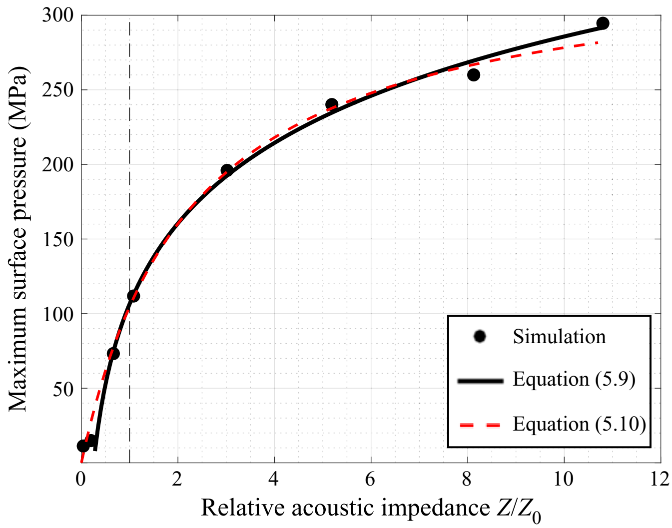

FIGURE 20. Effect of material's acoustic impedance on the maximum hydrodynamic pressure on material surface. Dashed line: $Z = Z_0$.

For the eight materials considered (with $Z/Z_0 \in [0.04, 10.8]$), $p_{w,max}$ is approximately a linear function of $\log(Z/Z_0)$. Using least-squares fitting, the relationship is given by

$$p^{(1)}_{w,max} = \rho c_0^2 \left[0.07 \log_{10}\left(\frac{Z}{Z_0}\right) + 0.0416 \right], \tag{5.9}$$

where c_0 denotes the speed of sound in the fluid. This fitting function is plotted in figure 20. Despite the simplicity, a linear function like (5.9) cannot capture the correct asymptotic behaviour as Z/Z_0 goes to infinity. Accounting for the case of $Z/Z_0 = \infty$ (i.e. a rigid wall), we find that $p_{w,max}$ can also be fitted using a bounded growth function,

$$p^{(2)}_{w,max} = \rho c_0^2 \frac{0.0591(Z/Z_0)}{1 + 0.4434(Z/Z_0)}, \tag{5.10}$$

which is also shown in figure 20.

5.6. *Effect of bubble's stand-off distance*

While the material's acoustic impedance dictates the reflection of shock wave at the material surface, the bubble's stand-off distance determines the time when the reflected shock waves reach and interact with the bubble, and hence, is an important parameter that affects the subsequent bubble dynamics. To study how the stand-off distance D_0 influences the material's reciprocal effects discussed above, we re-run the three representative cases presented in § 4 using different D_0 between R_0 and $6R_0$.

Table 9 compares the results obtained with a stand-off distance of $D_0 = 4R_0$ and the results for $D_0 = 2R_0$ from table 3. For both stand-off distances, similar trends in bubble's collapse time and the peak surface pressure with respect to Z/Z_0 can be observed. However, the differences between three materials in the case of $D_0 = 4R_0$ becomes smaller, indicating that the effect of nearby materials becomes weaker with increased stand-off distance. This is because it takes longer (i.e. approximately twice as the case of

Material	Bubble's collapse time (µs)		Maximum surface pressure (MPa)	
	$D_0 = 2R_0$	$D_0 = 4R_0$	$D_0 = 2R_0$	$D_0 = 4R_0$
BegoStone	0.306	0.327	255	96
Polyurea	0.335	0.335	119	53
SBR foam	0.465	0.346	No shock wave	22

TABLE 9. Comparison of the dynamics of bubble collapse with two stand-off distances ($D_0 = 2R_0$ and $D_0 = 4R_0$).

$D_0 = 2R_0$) for the reflected wave to reach and interact with the collapsing bubble, which thus weakens the material's effect on the collapse process. Another interesting observation is that because of the reduced effect from the nearby material, a shock wave is emitted in the case of the SBR foam with $D_0 = 4R_0$.

Furthermore, there exists a limit value of standoff distance, above which the bubble would reach its minimum volume before the reflection of the incident shock arrives, therefore its initial collapse is not affected by the solid material. Our numerical test suggests that for the current setting, the limit stand-off distance is approximately $D_0^* = 5.5R_0$.

We also find that (5.5) provides a good estimate of this limit stand-off distance. Specifically, the time for the shock wave to travel between the bubble and the material surface (back and forth) is given by

$$t_{wp} = \frac{2D_0}{c} = 2D_0\sqrt{\frac{\rho_l}{\gamma_L(p + p_L)}} \approx 2D_0\sqrt{\frac{\rho_l}{\gamma_L p_L}}, \tag{5.11}$$

where D_0 denotes the bubble's stand-off distance, γ_L and p_L are constant coefficients of the stiffened equation of state. At the limit stand-off distance, denoted by D_0^*, t_{wp} is equal to the bubble's collapse time, t_c. Combining (5.5) with $c_r = c_r^* = 0$ and (5.11) gives

$$2D_0^*\sqrt{\frac{\rho_l}{\gamma_L p_L}} = 0.915\sqrt{\frac{\rho_l}{p_i - p_v}}R_0\left(1 + 0.205\frac{R_0}{D_0^*}\right) \tag{5.12}$$

which is a quadratic equation of R_0/D_0^*. Solving this equation gives $R_0/D_0^* = 0.1809$, or equivalently, $D_0^* = 5.53R_0$, which matches well the result of our numerical test.

6. Summary and conclusions

Using a recently developed fluid–solid coupled computational model, we have analysed the collapse of a single bubble induced by a shock wave near different types of solid materials, including metals, minerals, glass, polymers and foams. By coupling the dynamics of the bubble, the ambient liquid, and the solid material, the computational model allowed us to investigate their interactions in detail. In this study, we have focused on elucidating the effects of the solid material's longitudinal acoustic impedance (Z) on the bubble and fluid dynamics, including the shock wave and liquid jet resulting from the bubble's collapse. We presented a detailed comparison of three representative cases with $Z/Z_0 > 1$, $Z/Z_0 \approx 1$, and $Z/Z_0 < 1$, respectively, where Z_0 is the acoustic impedance of the ambient fluid (water). Then, we expanded the study with five additional materials to cover a relatively broad range of Z/Z_0, that is, between 0.04 and 10.8. We investigated the effects of Z/Z_0 on the bubble's collapse time, the minimum bubble volume and the maximum hydrodynamic pressure on the material surface. We also designed and calibrated phenomenological models to capture these effects.

Several main findings of this study are noteworthy. First, the study reveals a two-way coupling between the fluids and the solid material: when the same bubble collapses near different materials (especially, materials with different acoustic impedance), the stress field inside the material, the bubble dynamics, the fluid pressure and velocity fields and the shock wave and liquid jet resulting from the bubble's collapse all vary. This finding indicates that modelling a material surface as a rigid wall may be inaccurate, even if the solid material has a Young's modulus on the order of tens of GPa. (see, e.g. figure 13). Second, the study shows that Z/Z_0 is a key parameter that dominates the material's reciprocal effect to the bubble and fluid dynamics, including the speed of bubble collapse and rebound, the speed of the liquid jet, and the emission (and amplitude) of the shock wave resulting from bubble collapse. This finding is supported both by a mechanistic study on the three representative cases with different values of Z, and a numerical parametric study of materials that have the same Z, yet differ in density, Young's modulus and Poisson's ratio. Third, the study shows that $Z/Z_0 = 1$ can be considered as a transition point. When $Z/Z_0 < 1$, the material surface reflects the compressive front of the incident shock wave as a tensile wave. The reflection reduces the speed of the bubble's collapse. As a result, the collapse produces a liquid jet, but not necessarily a shock wave. When $Z/Z_0 > 1$, the surface reflects the compressive shock front as a compressive wave. The reflection accelerates the bubble's collapse. As a result, the maximum pressure of the emitted shock wave increases linearly with $\log(Z/Z_0)$ (within the range mentioned above), and can be much higher than the amplitude of the incident shock. Interestingly, this emitted shock wave also gets reflected at the material surface, and the reflected wave slows down the liquid jet. More generally, this finding indicates that the mechanisms of cavitation-induced material damage may be related to the material's acoustic impedance. For materials with high acoustic impedance, our study indicates that the emitted shock wave may have a peak pressure of the order of 100 MPa. But for 'soft' materials with $Z < Z_0$, the bubble's collapse may not emit a shock wave. Instead, the high-speed liquid jet may become a mechanism of material damage.

A few limitations of this study should also be mentioned. The study considers a specific setting that features the collapse of an air bubble induced by a planar shock wave, while the viscous/viscoelastic effects of the surrounding liquid on the bubble collapse are neglected. The generality of the findings obtained for this setting – particularly, their validity under different conditions – requires further investigation. Also, although we commented on the mechanisms of cavitation-induced material damage based on the fluid pressure and velocity results, the numerical simulations do not directly predict material damage or fracture. Incorporation (and calibration) of material damage and fracture models is non-trivial, but possible (see, e.g. Cao *et al.* 2019). Furthermore, the phenomenological models proposed in § 5 can be generalized – for example, c_s and c_r should be functions of the bubble's stand-off distance. In our opinion, these are all worthwhile directions for future study.

Acknowledgements

The authors gratefully acknowledge the support of the National Science Foundation (NSF) under Awards CBET-1751487 and CBET-1706003, and the support of the Office of Naval Research (ONR) under Awards N00014-17-1-2831 and N00014-19-1-2102. The authors thank Drs Y. Zhang, Q. Zhan, and P. Zhong for their advice and assistant on the verification study, and Drs P. Avery and C. Farhat for their advice and assistance on the development and use of the computational model.

Declaration of interests

The authors report no conflict of interest.

Supplementary movies

Supplementary movies are available at https://doi.org/10.1017/jfm.2020.810.

REFERENCES

ABOUEL-KASEM, A., EL-DEEN, A. E., EMARA, K. M. & AHMED, S. M. 2009 Investigation into cavitation erosion pits. *J. Tribol.* **131** (3), 031605.

AMIRKHIZI, A. V., ISAACS, J., MCGEE, J. & NEMAT-NASSER, S. 2006 An experimentally-based viscoelastic constitutive model for polyurea, including pressure and temperature effects. *Phil. Mag.* **86** (36), 5847–5866.

ASHBY, M. F. 2010 *Materials Selection in Mechanical Design*. Butterworth-Heinemann.

BLAKE, J. R. & GIBSON, D. C. 1981 Growth and collapse of a vapour cavity near a free surface. *J. Fluid Mech.* **111**, 123–140.

BOUIX, R., VIOT, P. & LATAILLADE, J.-L 2009 Polypropylene foam behaviour under dynamic loadings: strain rate, density and microstructure effects. *Intl J. Impact Engng* **36** (2), 329–342.

BREKHOVSKIKH, L. M. & GODIN, O. A. 2012 *Acoustics of Layered Media I: Plane and Quasi-Plane Waves*, vol. 5. Springer Science & Business Media.

BREMS, S., HAUPTMANN, M., CAMEROTTO, E., PACCO, A., KIM, T.-G., XU, X., WOSTYN, K., MERTENS, P. & DE GENDT, S. 2014 Nanoparticle removal with megasonics: a review. *ECS J. Solid State Sci. Technol.* **3** (1), N3010–N3015.

BRENNEN, C. E. 2014 *Cavitation and Bubble Dynamics*. Cambridge University Press.

BRENNEN, C. E. 2015 Cavitation in medicine. *Interface Focus* **5** (5), 20150022.

BRUJAN, E.-A. 2019 Shock wave emission and cavitation bubble dynamics by femtosecond optical breakdown in polymer solutions. *Ultrason. Sonochem.* **58**, 104694.

BRUJAN, E. A., KEEN, G. S., VOGEL, A. & BLAKE, J. R. 2002 The final stage of the collapse of a cavitation bubble close to a rigid boundary. *Phys. Fluids* **14** (1), 85–92.

BRUJAN, E.-A. & MATSUMOTO, Y. 2012 Collapse of micrometer-sized cavitation bubbles near a rigid boundary. *Microfluid Nanofluid* **13** (6), 957–966.

BRUJAN, E.-A., NAHEN, K., SCHMIDT, P. & VOGEL, A. 2001 Dynamics of laser-induced cavitation bubbles near elastic boundaries: influence of the elastic modulus. *J. Fluid Mech.* **433**, 283–314.

CALVISI, M. L., ILORETA, J. I. & SZERI, A. J. 2008 Dynamics of bubbles near a rigid surface subjected to a lithotripter shock wave. Part 2. Reflected shock intensifies non-spherical cavitation collapse. *J. Fluid Mech.* **616**, 63–97.

CAO, S., ZHANG, Y., LIAO, D., ZHONG, P. & WANG, K. G. 2019 Shock-induced damage and dynamic fracture in cylindrical bodies submerged in liquid. *Intl J. Solids Struct.*

CHAHINE, G. L. & HSIAO, C.-T. 2015 Modelling cavitation erosion using fluid–material interaction simulations. *Interface Focus* **5** (5), 20150016.

CHENELER, D. 2016 Viscoelasticity of polymers: theory and numerical algorithms. *Appl. Rheol.* **26** (4), 10–52.

CHUNG, H., CAO, S., PHILEN, M., BERAN, P. S. & WANG, K. G. 2018 CFD-CSD coupled analysis of underwater propulsion using a biomimetic fin-and-joint system. *Comput. Fluids* **172**, 54–66.

CHURCH, C. C. 1989 A theoretical study of cavitation generated by an extracorporeal shock wave lithotripter. *J. Acoust. Soc. Am.* **86** (1), 215–227.

COUSSIOS, C. C. & ROY, R. A. 2008 Applications of acoustics and cavitation to noninvasive therapy and drug delivery. *Annu. Rev. Fluid Mech.* **40**, 395–420.

DEIGAN, R. J. 2007 Modeling and experimental investigations of the shock response of viscoelastic foams. PhD thesis, University of Maryland.

DULAR, M., DELGOSHA, O. C. & PETKOVŠEK, M. 2013 Observations of cavitation erosion pit formation. *Ultrason. Sonochem.* **20** (4), 1113–1120.

ESCH, E., SIMMONS, W. N., SANKIN, G., COCKS, H. F., PREMINGER, G. M. & ZHONG, P. 2010 A simple method for fabricating artificial kidney stones of different physical properties. *Urol. Res.* **38** (4), 315–319.

FARHAT, C., GERBEAU, J.-F. & RALLU, A. 2012 Fiver: a finite volume method based on exact two-phase Riemann problems and sparse grids for multi-material flows with large density jumps. *J. Comput. Phys.* **231** (19), 6360–6379.

FARHAT, C., RALLU, A. & SHANKARAN, S. 2008 A higher-order generalized ghost fluid method for the poor for the three-dimensional two-phase flow computation of underwater implosions. *J. Comput. Phys.* **227** (16), 7674–7700.

FARHAT, C., RALLU, A., WANG, K. & BELYTSCHKO, T. 2010 Robust and provably second-order explicit–explicit and implicit–explicit staggered time-integrators for highly non-linear compressible fluid–structure interaction problems. *Intl J. Numer. Meth. Engng* **84** (1), 73–107.

FARHAT, C., WANG, K. G., MAIN, A., KYRIAKIDES, S., LEE, L-H., RAVI-CHANDAR, K. & BELYTSCHKO, T. 2013 Dynamic implosion of underwater cylindrical shells: experiments and computations. *Intl J. Solids Struct.* **50** (19), 2943–2961.

FOLDS, D. L. 1974 Speed of sound and transmission loss in silicone rubbers at ultrasonic frequencies. *J. Acoust. Soc. Am.* **56** (4), 1295–1296.

FOVARGUE, D. E., MITRAN, S., SMITH, N. B., SANKIN, G. N., SIMMONS, W. N. & ZHONG, P. 2013 Experimentally validated multiphysics computational model of focusing and shock wave formation in an electromagnetic lithotripter. *J. Acoust. Soc. Am.* **134** (2), 1598–1609.

FREUND, J. B., SHUKLA, R. K. & EVAN, A. P. 2009 Shock-induced bubble jetting into a viscous fluid with application to tissue injury in shock-wave lithotripsy. *J. Acoust. Soc. Am.* **126** (5), 2746–2756.

GIBSON, D. C. & BLAKE, J. R. 1982 The growth and collapse of bubbles near deformable surfaces. *Appl. Sci. Res.* **38** (1), 215–224.

GOH, S. M., CHARALAMBIDES, M. N. & WILLIAMS, J. G. 2004 Determination of the constitutive constants of non-linear viscoelastic materials. *Mech. Time-Depend. Mat.* **8** (3), 255–268.

GUO, S., KHOO, B. C., TEO, S. L. M., ZHONG, S., LIM, C. T. & LEE, H. P. 2014 Effect of ultrasound on cyprid footprint and juvenile barnacle adhesion on a fouling release material. *Colloids Surf.* B **115**, 118–124.

DE HOOP, A. T. & VAN DER HIJDEN, J. H. M. T. 1984 Generation of acoustic waves by an impulsive point source in a fluid/solid configuration with a plane boundary. *J. Acoust. Soc. Am.* **75** (6), 1709–1715.

HUANG, D. Z., DE SANTIS, D. & FARHAT, C. 2018 A family of position-and orientation-independent embedded boundary methods for viscous flow and fluid-structure interaction problems. *J. Comput. Phys.* **365**, 74–104.

INRIA 2013 Gar6more3d. Available at: http://gar6more3d.gforge.inria.fr/.

JOHNSEN, E. & COLONIUS, T. 2008 Shock-induced collapse of a gas bubble in shockwave lithotripsy. *J. Acoust. Soc. Am.* **124** (4), 2011–2020.

JOHNSEN, E. & COLONIUS, T. 2009 Numerical simulations of non-spherical bubble collapse. *J. Fluid Mech.* **629**, 231–262.

KOBAYASHI, K., KODAMA, T. & TAKAHIRA, H. 2011 Shock wave–bubble interaction near soft and rigid boundaries during lithotripsy: numerical analysis by the improved ghost fluid method. *Phys. Med. Biol.* **56** (19), 6421.

KOCH, M., LECHNER, C., REUTER, F., KÖHLER, K., METTIN, R. & LAUTERBORN, W. 2016 Numerical modeling of laser generated cavitation bubbles with the finite volume and volume of fluid method, using openfoam. *Comput. Fluids* **126**, 71–90.

KODAMA, T. & TAKAYAMA, K. 1998 Dynamic behavior of bubbles during extracorporeal shock-wave lithotripsy. *Ultrasound Med. Biol.* **24** (5), 723–738.

KRÖNINGER, D., KÖHLER, K., KURZ, T. & LAUTERBORN, W. 2010 Particle tracking velocimetry of the flow field around a collapsing cavitation bubble. *Exp. Fluids* **48** (3), 395–408.

KUDRYASHOVA, O. & VOROZHTSOV, S. 2016 On the mechanism of ultrasound-driven deagglomeration of nanoparticle agglomerates in aluminum melt. *JOM* **68** (5), 1307–1311.

LI, F., YANG, C., YUAN, F., LIAO, D., LI, T., GUILAK, F. & ZHONG, P. 2018 Dynamics and mechanisms of intracellular calcium waves elicited by tandem bubble-induced jetting flow. *Proc. Natl Acad. Sci.* **115** (3), E353–E362.

MAEDA, K., MAXWELL, A. D., COLONIUS, T., KREIDER, W. & BAILEY, M. R. 2018 Energy shielding by cavitation bubble clouds in burst wave lithotripsy. *J. Acoust. Soc. Am.* **144** (5), 2952–2961.

MAIN, G. A. 2014 Implicit and higher-order discretization methods for compressible multi-phase fluid and fluid-structure problems. PhD thesis, Stanford University.

MAIN, A., ZENG, X., AVERY, P. & FARHAT, C. 2017 An enhanced fiver method for multi-material flow problems with second-order convergence rate. *J. Comput. Phys.* **329**, 141–172.

MÜLLER, S., BACHMANN, M., KRÖNINGER, D., KURZ, T. & HELLUY, P. 2009 Comparison and validation of compressible flow simulations of laser-induced cavitation bubbles. *Comput. Fluids* **38** (9), 1850–1862.

OHL, C.-D., ARORA, M., IKINK, R., DE JONG, N., VERSLUIS, M., DELIUS, M. & LOHSE, D. 2006 Sonoporation from jetting cavitation bubbles. *Biophys. J.* **91** (11), 4285–4295.

PHILIPP, A. & LAUTERBORN, W. 1998 Cavitation erosion by single laser-produced bubbles. *J. Fluid Mech.* **361**, 75–116.

PISHCHALNIKOV, Y. A., SAPOZHNIKOV, O. A., BAILEY, M. R., WILLIAMS, J. C. JR., CLEVELAND, R. O., COLONIUS, T., CRUM, L. A., EVAN, A. P. & MCATEER, J. A. 2003 Cavitation bubble cluster activity in the breakage of kidney stones by lithotripter shockwaves. *J. Endourol.* **17** (7), 435–446.

RATTRAY, M. 1951 Perturbation effects in cavitation bubble dynamics. PhD thesis, California Institute of Technology.

ROBINSON, P. B., BLAKE, J. R., KODAMA, T., SHIMA, A. & TOMITA, Y. 2001 Interaction of cavitation bubbles with a free surface. *J. Appl. Phys.* **89** (12), 8225–8237.

ROE, P. L. 1981 Approximate Riemann solvers, parameter vectors, and difference schemes. *J. Comput. Phys.* **43** (2), 357–372.

SANKIN, G. N. & ZHONG, P. 2006 Interaction between shock wave and single inertial bubbles near an elastic boundary. *Phys. Rev.* E **74** (4), 046304.

SHAW, S. J., SCHIFFERS, W. P., GENTRY, T. P. & EMMONY, D. C. 2000 The interaction of a laser-generated cavity with a solid boundary. *J. Acoust. Soc. Am.* **107** (6), 3065–3072.

SIMMONS, W. N., COCKS, F. H., ZHONG, P. & PREMINGER, G. 2010 A composite kidney stone phantom with mechanical properties controllable over the range of human kidney stones. *J. Mech. Behav. Biomed. Mater.* **3** (1), 130–133.

TOMITA, Y. & SHIMA, A. 1986 Mechanisms of impulsive pressure generation and damage pit formation by bubble collapse. *J. Fluid Mech.* **169**, 535–564.

TURANGAN, C. K., BALL, G. J., JAMALUDDIN, A. R. & LEIGHTON, T. G. 2017 Numerical studies of cavitation erosion on an elastic–plastic material caused by shock-induced bubble collapse. *Proc. R. Soc.* A **473** (2205), 20170315.

TURANGAN, C. K., ONG, G. P., KLASEBOER, E. & KHOO, B. C. 2006 Experimental and numerical study of transient bubble-elastic membrane interaction. *J. Appl. Phys.* **100** (5), 054910.

TURNER, S. E. 2007 Underwater implosion of glass spheres. *J. Acoust. Soc. Am.* **121** (2), 844–852.

VAN LEER, B. 1979 Towards the ultimate conservative difference scheme. V. A second-order sequel to Godunov's method. *J. Comput. Phys.* **32** (1), 101–136.

WANG, Q. 2014 Multi-oscillations of a bubble in a compressible liquid near a rigid boundary. *J. Fluid Mech.* **745**, 509–536.

WANG, K. G. 2017 Multiphase fluid-solid coupled analysis of shock-bubble-stone interaction in shockwave lithotripsy. *Intl J. Numer. Meth. Biomed. Engng* **33** (10), e2855.

WANG, K., GRÉTARSSON, J., MAIN, A. & FARHAT, C. 2012 Computational algorithms for tracking dynamic fluid–structure interfaces in embedded boundary methods. *Intl J. Numer. Meth. Fluids* **70** (4), 515–535.

WANG, K. G., LEA, P. & FARHAT, C. 2015 A computational framework for the simulation of high-speed multi-material fluid–structure interaction problems with dynamic fracture. *Intl J. Numer. Meth. Engng* **104** (7), 585–623.

WANG, K. G., LEA, P., MAIN, A., MCGARITY, O. & FARHAT, C. 2014 Predictive simulation of underwater implosion: coupling multi-material compressible fluids with cracking structures. In *ASME 2014 33rd International Conference on Ocean, Offshore and Arctic Engineering*, p. V08AT06A028. American Society of Mechanical Engineers.

WANG, K., RALLU, A., GERBEAU, J.-F. & FARHAT, C. 2011 Algorithms for interface treatment and load computation in embedded boundary methods for fluid and fluid–structure interaction problems. *Intl J. Numer. Meth. Fluids* **67** (9), 1175–1206.

XU, H., ZEIGER, B. W. & SUSLICK, K. S. 2013 Sonochemical synthesis of nanomaterials. *Chem. Soc. Rev.* **42** (7), 2555–2567.

ZHANG, S., DUNCAN, J. H. & CHAHINE, G. L. 1993 The final stage of the collapse of a cavitation bubble near a rigid wall. *J. Fluid Mech.* **257**, 147–181.

ZHONG, P. 2013 Shock wave lithotripsy. In *Bubble Dynamics and Shock Waves*, pp. 291–338. Springer.

ZHONG, P., ZHOU, Y. & ZHU, S. 2001 Dynamics of bubble oscillation in constrained media and mechanisms of vessel rupture in SWL. *Ultrasound Med. Biol.* **27** (1), 119–134.